2023-05-01

Metal Fused Filament Fabrication: Distortion Compensation & Co2 Electrochemical Reduction

Jean Emmanuel Montes Ramirez
University of Texas at El Paso

Recommended Citation

Montes Ramirez, Jean Emmanuel, "Metal Fused Filament Fabrication: Distortion Compensation & Co2 Electrochemical Reduction" (2023). *Open Access Theses & Dissertations*. 3828.
https://scholarworks.utep.edu/open_etd/3828

METAL FUSED FILAMENT FABRICATION: DISTORTION COMPENSATION & CO_2 ELECTROCHEMICAL REDUCTION

JEAN EMMANUEL MONTES RAMIREZ

Doctoral Program in Mechanical Engineering

APPROVED:

Yirong Lin, Ph.D., Chair

Tzu-Liang Tseng, Ph.D., Co-Chair

Zhengtao Gan, Ph.D.

Joel Quintana, Ph.D.

Stephen L. Crites, Jr., Ph.D.
Dean of the Graduate School

Dedication

I would like to dedicate this work to my loving family, who has always been there for me throughout my academic journey. Your unwavering support and encouragement have been an immense motivator for me to pursue my goals and dreams. I am forever grateful to my hardworking father, who has provided me with countless opportunities and guided me along the way with his wisdom and experience. My diligent mother, who has always been there to take care of me, has taught me the values of respect, honesty, compassion, and perseverance, which have shaped me into the person I am today. To my beloved brothers, I owe a debt of gratitude for their unwavering support, guidance, and encouragement throughout my academic journey. Their presence has been a constant source of inspiration, and their unwavering commitment to my success has been an invaluable asset to me. To my dearest fiancé, words cannot express how grateful I am for your unwavering support and encouragement throughout this journey. Your love and motivation have been the driving force behind my success, and I am truly blessed to have you by my side. I am grateful for your constant support and encouragement.

To everyone who has been a part of my journey, I dedicate this work to you. Your unwavering support, understanding, and encouragement have been invaluable, and I could not have reached this point without you. I hope this work reflects the love and gratitude I have for each and every one of you, and that it inspires others to pursue their passions and dreams with the same level of dedication and determination that you have shown me.

METAL FUSED FILAMENT FABRICATION: DISTORTION COMPENSATION & CO_2 ELECTROCHEMICAL REDUCTION

by

JEAN EMMANUEL MONTES RAMIREZ, M.S.

DISSERTATION

Presented to the Faculty of the Graduate School of
The University of Texas at El Paso
in Partial Fulfillment
of the Requirements
for the Degree of

DOCTOR OF PHILOSOPHY

Department of Aerospace and Mechanical Engineering
THE UNIVERSITY OF TEXAS AT EL PASO
May 2023

Acknowledgements

I want to express my sincere gratitude to my advisor, Dr. Yirong Lin, for his unwavering support, guidance, and encouragement throughout my graduate studies. Dr. Lin has been an inspiration to me, a role model in the field, and an exceptional mentor who pushed me to move forward and always strive for excellence. His vast knowledge and expertise in the field have been invaluable to my research, and I am deeply grateful for his continuous support, motivation, and patience.

I would also like to extend my gratitude to my committee members, Dr. Tzu-Lian Tseng, Dr. Zhengtao Gan, and Dr. Joel Quintana, for their invaluable feedback and insightful suggestions during the preparation and defense of my dissertation. Their critical insights and constructive criticisms have helped me to shape my research and improve the quality of my work.

Furthermore, I would like to express my gratitude to my peers, Joseph Munoz, Sahid Hassan, Cory Marquez, Alexis Lopez, Dante Favela, Sofia Gomez, and everyone in the SMP team, who have been supportive of me throughout my research journey. Your friendship, encouragement, and collaboration have helped me to grow not only as a researcher but also as a person. Thank you so much for all the support and help you've given me during my academic journey. Although I will be graduating and moving on to future endeavors, I am hopeful for the opportunity to work with you again in the future.

Table of Contents

List of Tables

List of Figures

Chapter I: Shrinkage and Deformation Compensation in Metal Fused Filament Fabrication (MF3) Sintered Copper Components using 3D Scanning and Inverse Deformation.

Section 1.1. Abstract

Metal Fused Filament Fabrication (MF3) is an emerging additive manufacturing technology which is gaining popularity due to its non-toxic & cost-effective materials/manufacturing process. Fused Filament Fabrication (FFF) is an additive manufacturing technology where material is extruded through a nozzle and deposited layer by layer until a final part is fabricated. FFF novel technique, namely MF3, involves material extrusion of a filament blend of metal powder with a thermoplastic binder which is later debinded and sintered to obtain a fully metal part. MF3 has many applications including medical prosthetics, medical implants, automobile, aerospace, and sensors. Current challenges involve geometry accuracy after debinding and sintering. Sintered parts tend to shrink and deform after densification. To characterize and further compensate for such deformation is key. The present research article involves digitally scanning the sintered part to generate a stereolithography (STL) file, which is subsequently compared to the original STL. Later, a pre-distorted inverse deformed model is designed, 3D printed, debinded, sintered, and scanned which results in a sintered part that is dimensionally accurate to the original STL.

Section 1.2. Introduction

Fused Filament Fabrication (FFF) is an additive manufacturing technique that extrudes thermoplastic filament through a heated nozzle, melting it briefly before laying it layer by layer to create a green part. FFF technology is widely favored due to its affordability, quick processing, minimal material wastage, user-friendly interface, accurate management of processing parameters, capacity to manufacture intricate components, and its ability to work with multiple materials [1] [2] [3]. Despite being a relatively low-cost additive manufacturing process compared to others, FFF has limited applications in the production of functional parts for global manufacturing efforts. Several factors contribute to this limitation, including poor part properties, a limited selection of raw materials, low printing temperature (500°C), size restrictions, and low production rates [4]. Yet, new materials are being developed to overcome the limitations of FFF technology enabling the fabrication of metals and ceramics components using Metal Fused Filament Fabrication (MF3) technology [4].

Similarly, to FFF, MF3 is an innovative technique that combines thermoplastic binder with metal powder to fabricate a composite metal filament that can then be 3-D printed using the FFF printing technique. Today, commercially available polymeric filaments that are blended with metallic powders such as Inconel, titanium, bronze, Stainless steel, aluminum, copper and other metals have made it easy and affordable to fabricate 3D metal objects using off-the-shelf 3D printers [5]. MF3 fabricated parts that are 3-D printed using FFF without any post-processing are called green parts. The green part has the binder's mechanical and thermal properties, and thus needs to be post-processed to obtain a fully metal part with the mechanical and thermal properties of the metal. Post-processing involves the printed parts undergoing debinding (brown part) and sintering (white part) processes to transform them into fully compact metal parts [6]. While metal additive manufacturing techniques that utilize metal powder, such as Powder bed Fusion (PBF), Direct Metal Sintering (DMLS), Electron Beam Melting, Binder Jetting (BJ), and Selective Laser Melting (SLM), can yield superior mechanical properties and offer a wide range of material selection, they are expensive and challenging to implement due to their high-energy processes, atmospheric controls to prevent oxidation, and strict powder property requirement for printability [2] [7] [8], [9]. In contrast, MF3 offers the advantages of FFF technology for low-cost, non-toxic, user-friendly, and low-maintenance for the fabrication of metal parts [2] [10].

As previously mentioned, debinding and sintering are crucial steps in the process. The debinding process is critical to remove the unwanted polymer matrix from the metal powder. Debinding in the MF3 process involves heating the printed part until a suitable temperature is reached where the polymer binder material can degrade and escape the part. As a result, the brown part is in a very fragile state due to the absence of material which left voids/pores throughout the brown part [6]. To densify the debinded part, sintering is employed. During the sintering process, the brown part is subjected to higher temperatures that reaches close to the melting temperature where fusion happens. This allows the part to almost densify completely [2] [6]. As MF3 technology continues to be studied, there are still many challenges that are present when using this technology. This work focuses on addressing two primary concerns, the shrinkage/post-deformation and oxidation that arise in copper MF3 printed parts caused by the debinding and sintering in air environment.

In additive manufacturing, distortion compensation refers to the process of minimizing and correcting deformation or warping that happens during the printing or post-processing steps of objects produced using 3D printing technology [11]. This is crucial if the printed material is to be precise and adheres to predetermined geometric and dimensional tolerances. To accomplish this, pre-distorted models are developed to anticipate and account for deformations brought on by the manufacturing or post-processing of such parts [12] [13]. Variables like material characteristics, temperature, processing conditions, and printing speed are used to adjust and guarantee that the final product meets the required specifications. To produce high-quality parts, reduce the need for machining, and boost the effectiveness of the additive manufacturing process, distortion compensation is a vital step [14].

Distortion Compensation is often used on high-end additive manufacturing processes such as Laser Powder Bed Fusion and Binder Jetting which are used to fabricate high precision parts. These technologies often produce distorted parts due to thermal stresses and high sintering temperatures [15] [13]. When de-binding and sintering a 3D printed part through binder jetting, the binder material is first removed through a de-binding process, which involves the removal of the organic binder material from the green part. Once the binder material is removed, the remaining part is called the brown part, which is then subjected to a sintering process to fuse the metal powder particles together to form a solid, dense part [16] [17].

The brown portion must be heated throughout the sintering process to a temperature near the metal's melting point. As a result, diffusion, and solid-state bonding work together to fuse the metal particles together. The metal may distort and warp because of this process' heat expansion and contraction, though. The volume of the fused metal structure will also decrease which may be made worse by the metal structure's inherent porosity. Further contraction happens as the pores close, and the amount of shrinkage and deformation depends on how the heat is distributed across the bulk. Popular software like Simufact Additive or Ansys Additive Suite can be used to create models that precisely forecast component deformation during the sintering process. These models can be used to account for the well-known manufacturing and post-treatment impacts on diverse materials [15] [18] [19].

3D printed copper has a wide range of applications where complex geometries with high electrical and thermal conductivity are important [5]. To retain the geometry of the sintered part is complicated and several variables are taken into account when the part densifies including shrinkage, friction, gravity, and buckling [20]. For this purpose, this research proposes to use sacrificial carbon to shield the green copper part from oxidation in an air environment. Additionally, an inverse pre-distorted model that employs 3D digital scanning will be used to evaluate the shrinkage effects and dimensional distortions of a sintered copper reverse U part, with the goal of generating an inverse pre-distorted STL file that will precisely match the original digital model dimensionally after sintering.

Section 1.3. Materials and Methods

Section 1.3.1. Materials and equipment

The multicomponent filament was composed of a polymer binder and copper particles. The copper filament (The Virtual Foundary, Stoughton, WI) had a diameter of 1.75 mm in a 1kg spool which contained 87.0% - 90.7% metal with a density of 4.8 g/cc - 5.0 g/cc. The 3D printer used to fabricate the parts was from Raise3D E2 printer (RAISE3D, Irvine, CA) with a print volume of 330 x 240 x 240 mm. Max build plate and nozzle temperature are 110 °C and 300 °C respectively. The debinding and sintering process was carried out using Deltech Furnace DT-31-FL-8-E3504 Front Load Furnace (Deltech Furnaces, USA) and sintering carbon (The Virtual Foundary, Stoughton, WI) to shield the part from oxidation. The debinding and sintering was performed at air environment and the schedules can be seen in table 1.1.

Table 1.1. Debinding and sintering schedule parameters.

	Ramp rate	**Target temperature**	**Dwell time**
Debinding	1 °C/min	482ºC	4 hours
Sintering	2 °C/min	1052ºC	5 hours

Section 1.3.2. Part fabrication

3D printed parts were designed on Fusion 360 (Autodesk, USA) and sliced using Ideamaker (version 4.4.0 Alpha) 3D slicer software. This machine has a direct drive extruder with a brass nozzle which was replaced by a hardened steel nozzle with a diameter of 0.6 mm to prevent clogging. The test specimen used was a reverse U geometry chosen based on simplicity and deformation caused by the overhang, thickness, and height. All specimens were printed using a rectilinear infill pattern with three perimeter shells, and 100% infill density. The reverse U was printed flat in the printing bed and the reference orientations for deviation can be in figure 1.1. Printing parameters can be found in table 1.2.

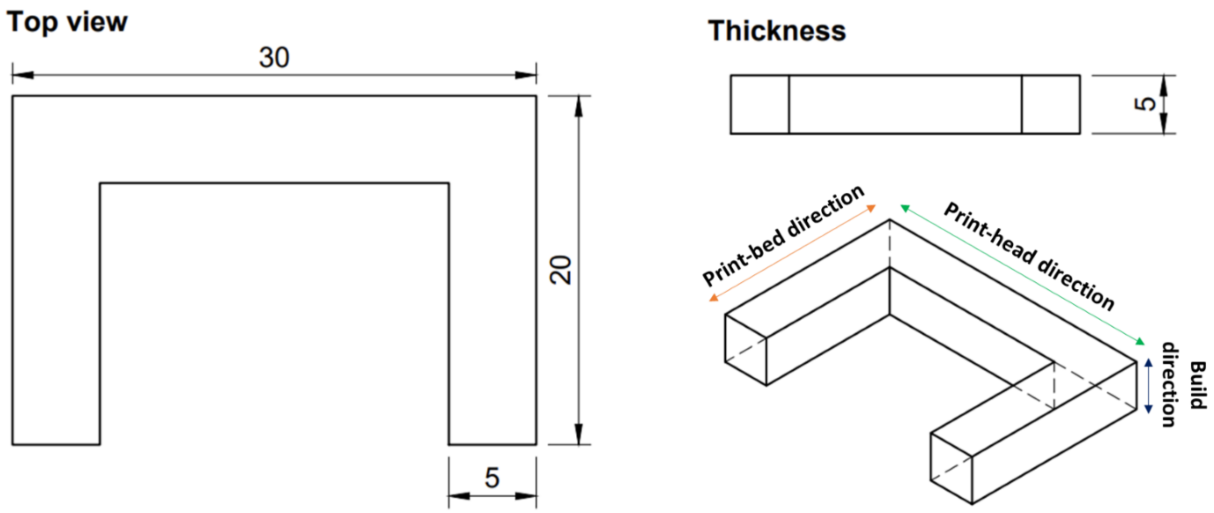

Figure 1.1. Original part dimensions and printing orientation

Table 1.2. Printing parameters

Nozzle temperature (°C)	Bed temperature (°C)	First layer height (mm)	Layer height (mm)	Nozzle speed (m/s)	First layer extrusion width percentage (%)
247	65	0.12	0.2	47	125

To obtain a fully compacted copper part, the 3D-printed green copper part underwent post-processing which included debinding and sintering. The whole fabrication process can be observed in figure 1.2.

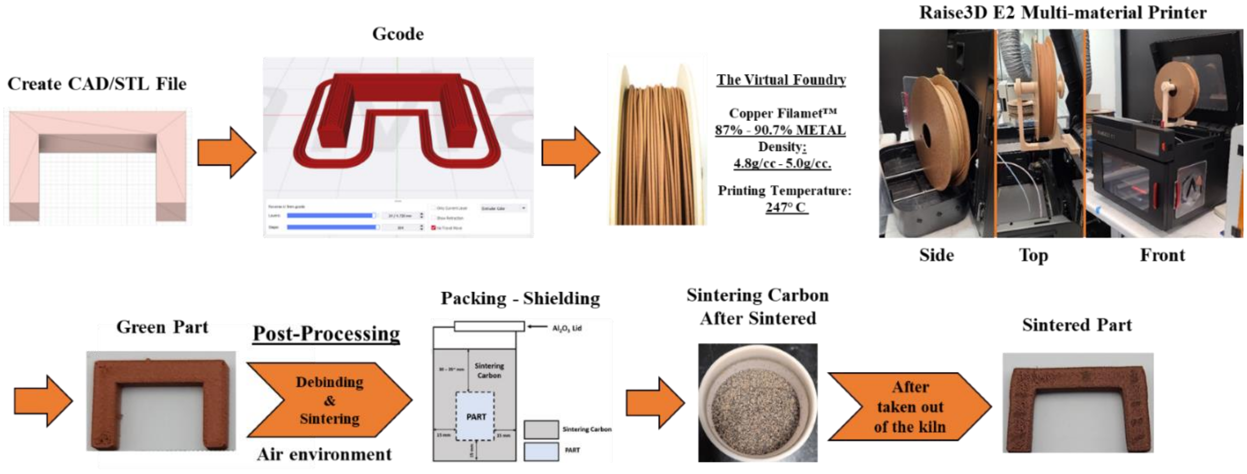

Figure 1.2. MF3 manufacturing process schematic

Section 1.3.3. Debinding

To perform the debinding process, packing was done by placing the 3D green part inside an Al_2O_3 crucible, subsequently, adding sacrificial carbon (The Virtual Foundary, Stoughton, WI) to protect the printed parts from oxidation in the ambient air. Additionally, a lid was placed on top while leaving an opening to limit the amount of carbon that will be used, since less carbon pellets were exposed. The debinding schedule parameters included a ramp rate of 1°C/min, a target temperature of 482°C, and a dwell time of 4 hours, as previously stated. The debinding process facilitates the removal of binder material from the part by heating. Any residual binder material can be eliminated during the sintering process. The debinding packing process can be visualized in Figure 1.3.

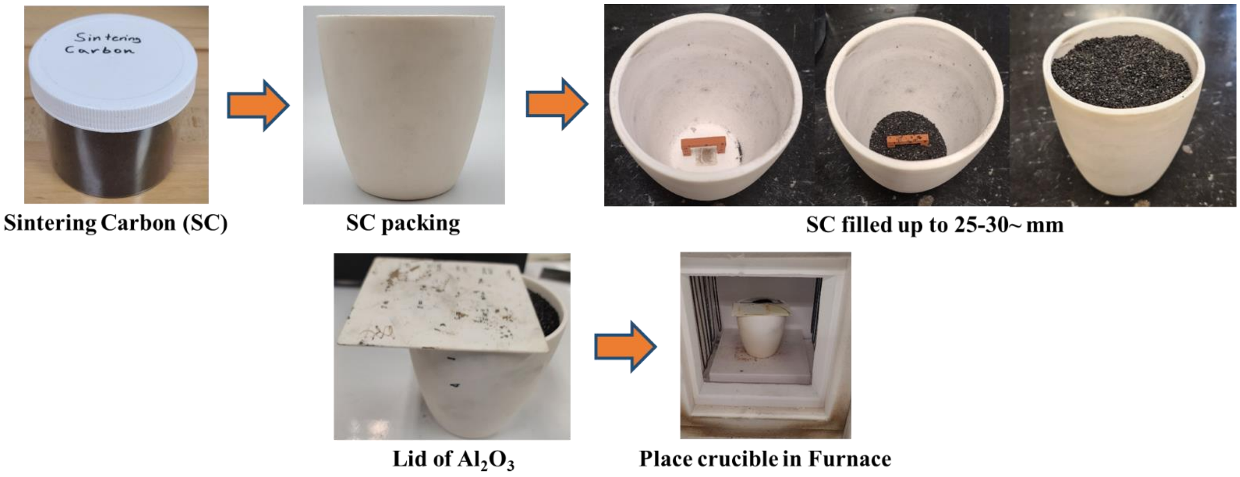

Figure 1.3. MF3 debinding/sintering packing process.

Section 1.3.4. Sintering

The debound parts underwent sintering, employing a ramp rate of 2°C/min, a target temperature of 1052°C, and a dwell time of 5 hours. Once sintered, the parts were cooled to room temperature under ambient air conditions. Similarly, the sintering packing process is followed in the same way as the debiding packing process. A schematic of the debinding/sintering process can be seen in Figure 1.4.

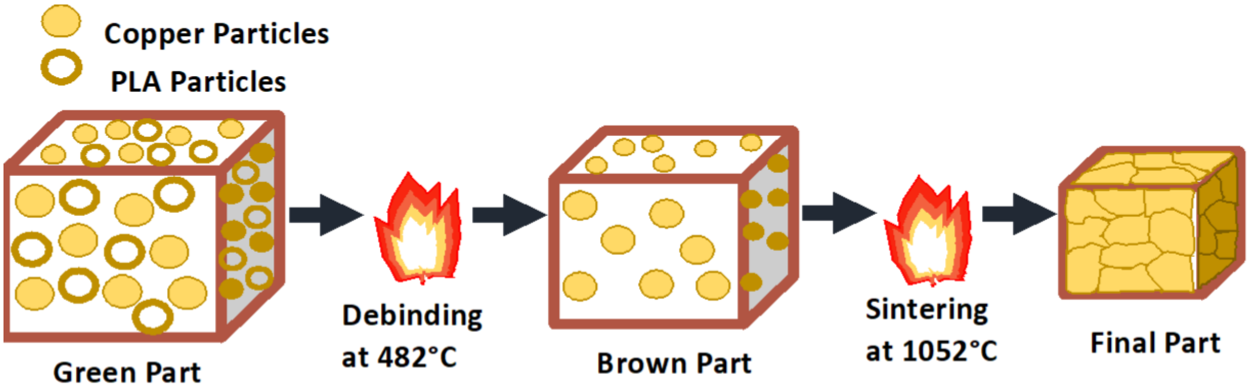

Figure 1.4. MF3 debinding and sintering manufacturing process schematic

Section 1.3.5. Characterization

To analyze the density, grain size, microstructure, composition, and geometrical accuracy of the sintered parts, several characterization techniques were employed, including Gravimetric analysis, metallography, Optical Microscope, X-Ray Diffraction (XRD) and digital scanning.

Section 1.3.5.1. Density analysis

An Archimedes Principle-based apparatus equipped with a TDK03 kit and a Sartorius model QUINTIX613-1S (Thermo Fisher Scientific, Waltham, MA, USA) was utilized to determine the density of the sintered specimens. The density was calculated by measuring the weight of the part in air and water (in accordance with ASTM Standard B962-15) [21]. All sintered samples underwent debinding and were subjected to the same heating schedule.

Section 1.3.5.2. X-Ray Diffraction

X-Ray diffraction (XRD) analysis was performed on 3 different sintered copper surfaces to assess the shielding effectiveness of sintering carbon. X-ray diffraction (XRD), using CuKα radiation on a DISCOVER diffractometer (Bruker, Boston, MA, USA) was used to perform the analysis.

Section 1.3.5.3. Optical Microscope

Optical microscopic images were obtained using digital imaging with a VFX-970F Keyence Digital Microscope (Keyence, Itasca, IL, USA). The samples were analyzed at a magnification ranging from 20-500X and porosity area was measured with the Keyence measuring tool.

Section 1.3.5.4. Metallography

The metallographic sample was prepared by grinding the sample at 180 grit paper to 600 grit. The polishing media used was Monocrystalline Diamond Suspension, which was done in three steps starting with 6 µm, 3µm and 1µm. Potassium Dichromate etching for 15-20 seconds revealed the microstructure of the MF3 Copper. Subsequently, the Olympus Optical Microscope GX53 (Olympus Corporation, Japan) was used to obtain the micrographs. The average grain size was calculated using equation 1 and determined through the line intercept method, which was measured by avoiding the pores to attain the most accurate value. A comparison of pore size relative to the microstructure area was conducted for pore size analysis. Pore size analysis was done using ImageJ software by converting the image type to 8-bit mask, adjusting the threshold to black & white then using the analyze particles option.

$$Average\ Grain\ Size = \frac{Total\ line\ length}{\#\ of\ intercepts} \qquad [1]$$

Section 1.3.5.5. Digital scanning

To achieve the purpose of this investigation, the distortion compensation process was carried out. After the sintering process, the printed part is taken out of the furnace and scanned with the Shinning 3D EinScan-SP Desktop, which generates an STL file. The STL is then imported into the GOM Inspect software, which provides a comparison between the nominal CAD model with the desired dimensions and the 3D scan. This software enables the observation of the distortion compensation and stress behavior under the debinding and sintering temperatures. By analyzing these stresses and distortions, the required displacements to correct for deviations from the nominal CAD model can be determined and applied to a new CAD model, which is modified using software such as Fusion 360. The modified CAD model is then reprinted, undergoes the sintering process again, and the cycle is repeated to evaluate the new deviations as seen in Figure 1.5. The findings obtained were subsequently assessed to evaluate the geometrical accuracy and properties of the sintered parts.

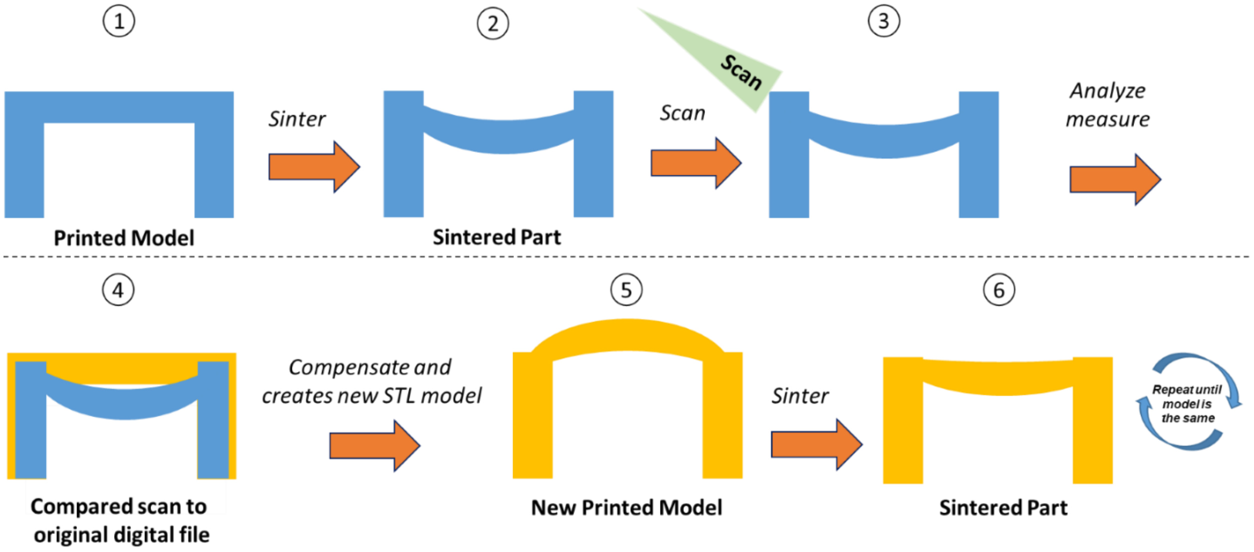

Figure 1.5. Digital scanning schematic. Printed model (1), sintered part (2), scan (3), compared scan to original digital file (4), inverse compensated printed model (5), and sintered part (6).

Section 1.4. Results and Discussion

Section 1.4.1. Density Analysis

To evaluate the efficiency of the sintering process, gravimetric analysis was conducted on reverse U sintered parts with 100% infill, and their densities were recorded, as illustrated in Figure 1.6. The results showed that the average density of the sintered reverse U parts was 7.88 g/cm3, which is lower than the ideal fully dense copper at room temperature (8.96 g/cm³), but is consistent with literature on sintered copper parts [22]. During the debinding process, the binder melts and evaporates exiting the part which leaves gaps and pores in the sintered part which leads to lower densities [23]. The lower densities observed in the original sintered part can be attributed to higher distortion, which resulted in more internal voids. Overall, the sintered parts achieved densities ranging from 7.65 to 8.03 g/cm3, which are consistent with dense sintered copper parts [24].

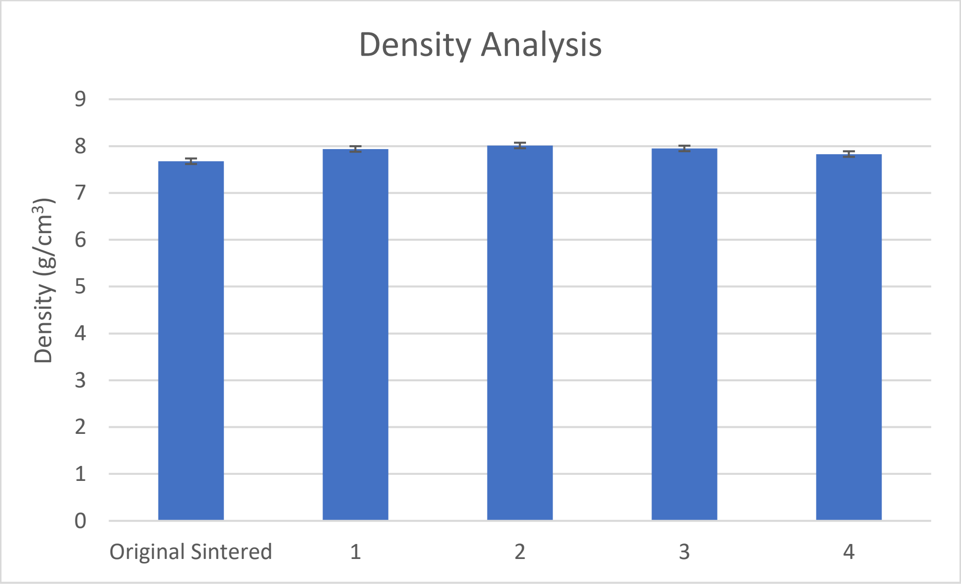

Figure 1.6. Density measurements of sintered reverse U iterations.

Section 1.4.2. Optical Microscope

Digital images were captured at magnifications ranging from 20-500X to evaluate the pore size and microstructure of the sintered specimens. Porosity is a critical quality factor that has a direct impact on the mechanical properties of the samples [25]. While mechanical properties are not the main focus of this study, it is important to note that porosity can affect the density of the sintered part and contribute to additional defects such as warping, shrinkage, and deformation after sintering.

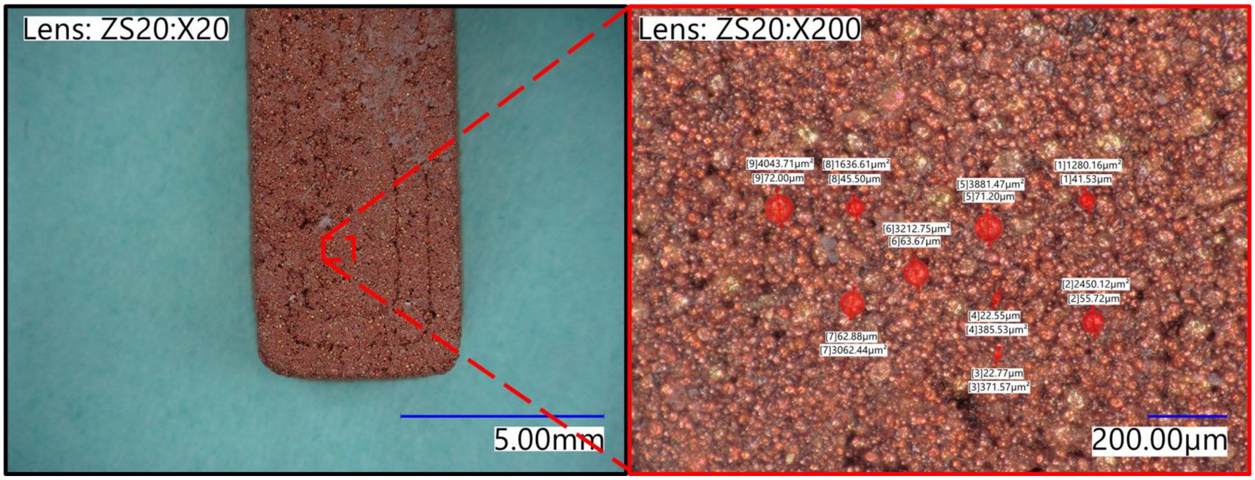

Figure 1.7. Digital optical microscope image at 20-200X magnification. Reverse U green part. Particle measurements.

Table 1.3. Reverse U green part particle size diameter and area analysis.

Particle Number	Particle Diameter (µm)	Particle Area (µm^2)	Particle Number	Particle Diameter (µm)	Particle Area (µm^2)
1	41.53	1280.16	6	63.67	3212.75
2	55.72	2450.12	7	62.88	3062.44
3	22.77	371.57	8	45.5	1636.61
4	22.55	385.53	9	72	4043.71
5	71.2	3881.47	Average	50.87	2258.26

Figure 1.7. displays a microscopic image of the reverse U-shaped green part with minimal porosity, as the pores are filled with the thermoplastic matrix that maintains the integrity of the body. The porosity of the green body can be attributed to various factors such as defects, nozzle size, printing parameters, lack of extrusion multiplier, and resolution of the 3D printer, which may result in porosity between adjacent layers [23]. In addition, particle diameter was measured which ranged from 22.55 um to 71.2 um. Particle sizes and corresponding areas measured can be observed in table 1.3.

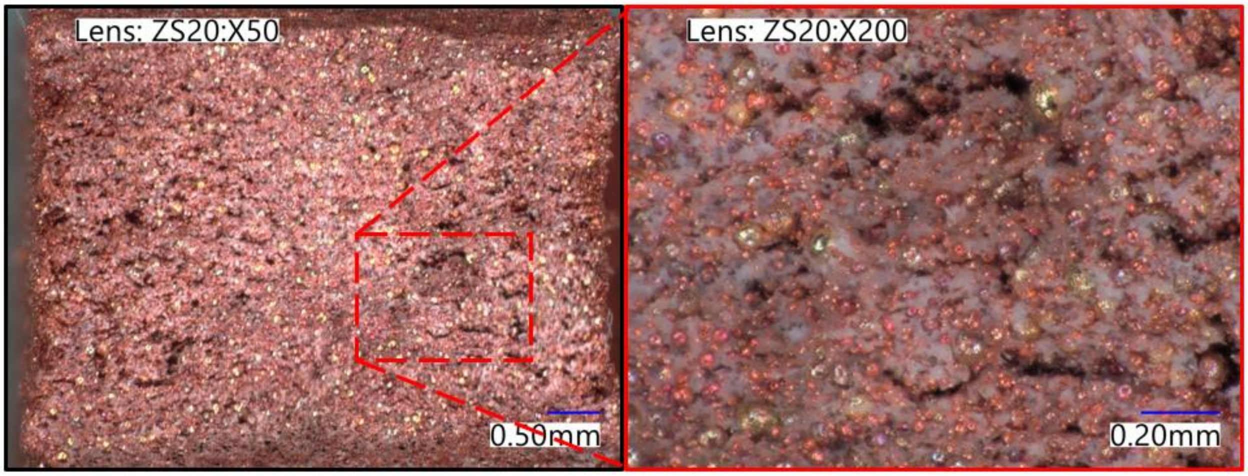

Figure 1.8. Digital optical microscope image at 20-200X magnification. Cross section of Reverse U green part.

In addition, the cross section of a green body was investigated and can be seen in Figure 1.8. The cross section shows the copper particles suspended in the thermoplastic binder matrix; however, the thermoplastic is smeared due to the sample being cut with a diamond saw. The thermoplastic being ductile causes it to smear across the sample. Moreover, copper particles of comparable sizes are visible, akin to those depicted in Figures 5 and 6. Finally, uniform dispersion of copper particles can be seen throughout the entire 3D-printed component.

Figure 1.9. showcases the microstructure, pore sizes, and pore areas of the sintered reverse U sample. The observed porosity in the micrographs is attributed to the printing parameters and the debinding/sintering schedule. In printing parameters, the porosity of the sintered body can be controlled to some extent by adjusting the infill percentage parameter in the gcode. Ait-Mansour et al., demonstrated the strong correlation between infill percentage and the sintered part [26]. For instance, setting the theorical infill percentage to 50% can result in a density of 55%, whereas 100% theorical infill percentage can achieve a density of 80-85%. This supports the reason for observing minimal porosity since 100% infill was utilized. Porosity attributed to debinding is

explained by [27] [28]. The process involves two stages: initially, the internal pressure of the liquid polymer increases, causing it to flow from the interior to the outer surfaces, where it degrades and escapes; subsequently, the remaining liquid polymer in the interior continues to degrade into vapor and flows to the outer surfaces via convection and diffusion [23]. Due to the mechanism at which the polymer escaped the part, provides the porosity and voids that can be seen. In addition, sintering ramp rate and set temperature play an important role in the densification of the part [23]. Table 1.4. shows the recorded pore sizes and areas at two different magnifications: 200 and 500X, respectively. The pore size diameter recorded ranged from 5.42 um to 21.21 um with an average pore size diameter of 15.44 um. Lastly, the presence of sintering carbon used in the process may explain the black glossy surface observed in some of the pores.

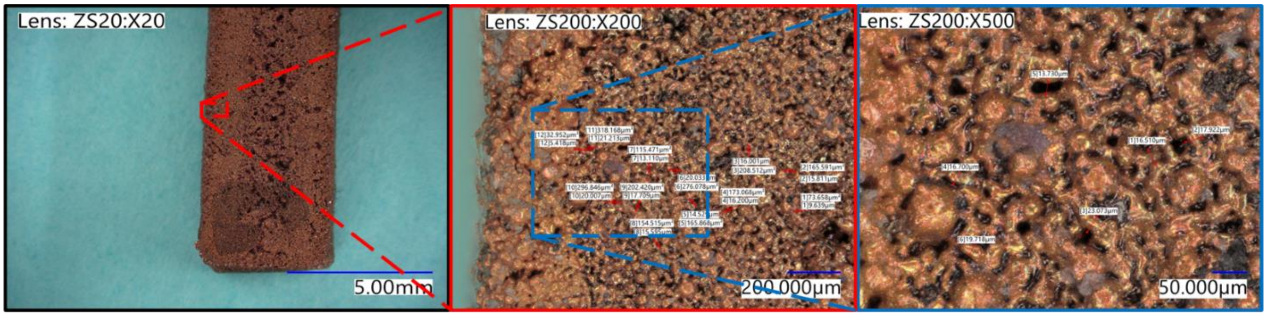

Figure 1.9. Digital optical microscope image at 20-500X magnification. Reverse U sintered part.

Table 1.4. Reverse U sintered part pore size diameter and area analysis.

Magnification: 200x						**Magnification: 500X**	
Pore Number	Pore Diameter (µm)	Pore Area (µm^2)	Pore Number	Pore Diameter (µm)	Pore Area (µm^2)	Pore Number	Pore Distance (µm)
1	9.64	73.66	7	13.11	115.47	1	16.51
2	15.81	165.59	8	15.60	154.52	2	17.92
3	16.00	208.51	9	17.71	202.42	3	23.07
4	16.2	173.07	10	20.01	296.85	4	16.7
5	14.53	165.87	11	21.21	318.17	5	13.73
6	20.03	276.08	12	5.42	32.95	6	19.72
Average	15.44	181.93				Average	17.94

Section 1.4.3. Metallography

The green part of the sample has not undergone sintering, resulting in the presence of metallic particles within the polymer matrix. The blurriness of the images is due to the microscope's inability to capture the depth of the pores. Copper particles can be seen surrounding the polymer matrix or binder that is observed in Figure 1.10.[a-b]. After sintering, a drastic change in the morphology of the Mf3 part can be examined in Figure 1.10.[c-d]. The as-polished condition will not reveal any grains until it has been etched, only porosity is seen in these images, hence porosity analysis is ideal in this microstructural state. These micrographs demonstrate the formation of twin boundaries common in FCC structures that have a mirror image on the same crystal lattice seen in Figure 1.10.[e-f] [29] [30]. This statement is supported with the XRD FCC structure of the copper. Sintering leads to incomplete visibility of grains, resulting in the formation of partial-like grains due to coalesced particles, ultimately leading to pore formation [31] [32]. Porosity is typically inversely related to grain size as sintering time and temperature has a significant effect on pore formation [33] [34]. In addition, a major drawback of sintering is the high porosity percentage that leads to undesired mechanical properties. But it can be managed by altering the parameters of the sintering process. By using ImageJ and narrowing down the pores by selecting the threshold and particle analyzer in Figure 1.10.[g-h], the pore size data was then automatically tabulated. The average pore size is 27.1µm, the pore count is estimated at 167414.1 hence the total average pore area relative to the entire microstructure is 18.12%.

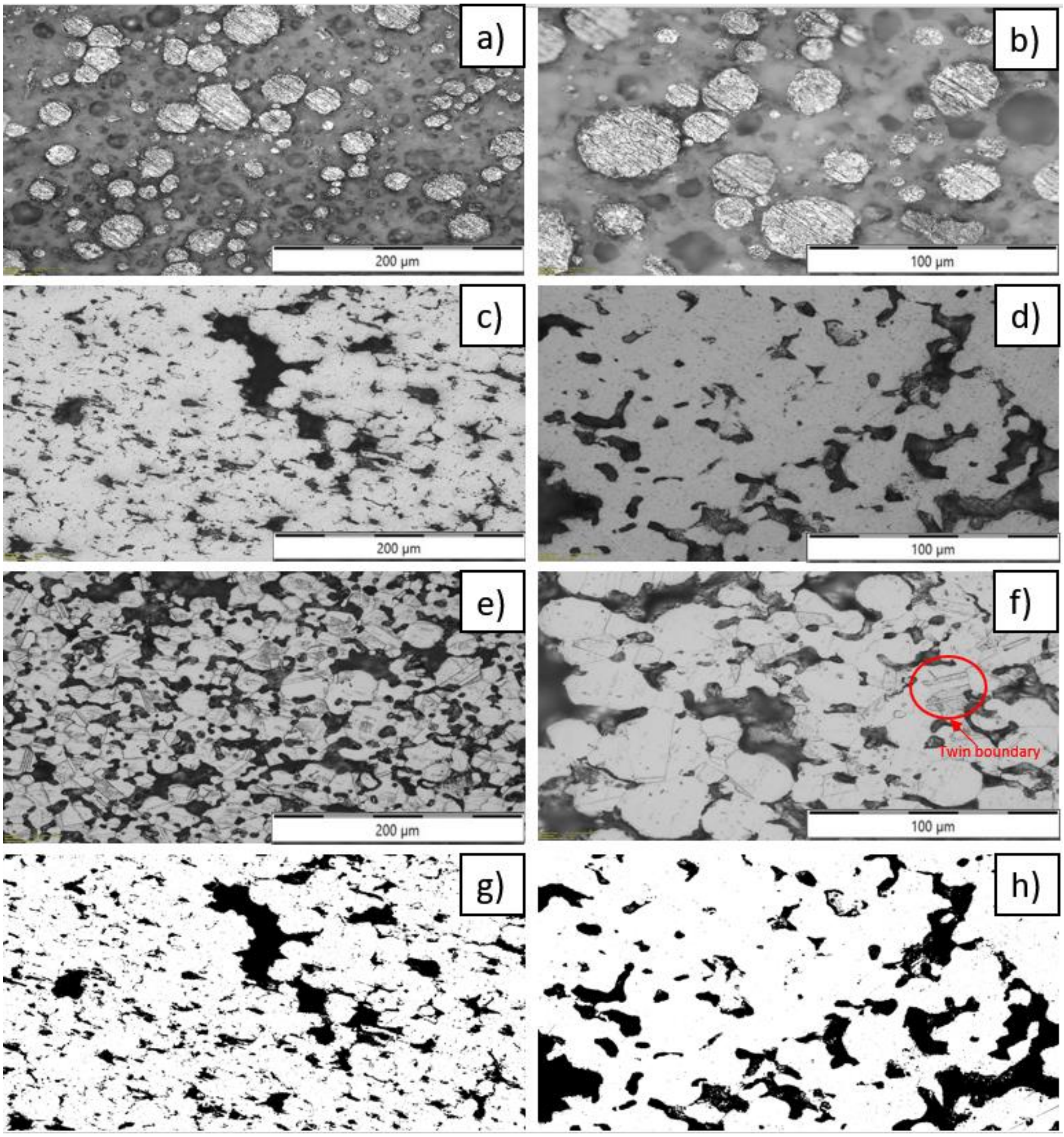

Figure 1.10. a) Green part at (100x), b) Green part at (200x), c) As-polished condition of Sintered Copper microstructure at (100x), d) As-polished condition of Sintered Copper microstructure at (200x) e) Sintered Copper microstructure at (100x), f) Sintered copper microstructure at (200x), g) Porosity analysis in the as-polished condition at (100x), f) Porosity analysis in the as-polished condition at (200x)

Table 1.5. Average Grain Size, using line intercept method.

Line Intercept	Line Length (µm)	# of Intercepts	Average Grain Size (µm)
1	353.26	7	48.12
2	239.74	8	48.85
3	230.93	4	54.58
4	321.88	8	64.60
5	252.11	3	47.32
6	290.55	6	46.18
7	265.77	6	50.92
Total Average	**2044.23**	**42**	**48.67**

The average grain size due to the coalescing nature of particles during the sintering process showed to have an Austenitic microstructure that have similar resemblance to classic copper microstructures. The average grain size calculations had to be done avoiding the pores best as possible to attain an accurate measurement. By using seven-line intercepts, 74 grains were intercepted along the total line length of 3756.19 µm, resulting in an average grain size of 50.76 µm.

Section 1.4.4. X-Ray Diffraction

Three different XRD analysis were conducted for each individual surface of the sample to view the crystallinity phases dependent on post-process treatment. Figure 1.11. shows three different surfaces of sintered Cu samples which have individually been treated differently. Figure 1.11.a shows an image of a sintered Cu surface which was polished using a DREMEL 4000 (Robert Bosch Tool Corporation, Mt. Prospect, IL) to remove all the impurities left in the surface of the sintered part. The XRD results show crystallinity peaks of Cu in 2θ 43, 50, and 74° which represent

(111), (200), and (220) for crystalline orientations respectively and are standard for Cu results that are sintered [35]. Figure 1.11.b shows the surface of a sintered unpolished sample that was untouched after sintering showing XRD results with small oxidation peeks forming in 2θ 35.5º corresponding to crystalline orientation of (-111) that occur during the preheating energy during sintering [36]. Figure 1.11.c shows an image of a heavily oxidized Cu surface which shows a visible indication of oxidation as the printed part was placed in a crucible where a sintered copper part had previously been oxidized. XRD analysis in Figure 1.11.c shows an increase in the peak of Cu oxidation which is caused from higher temperature exposures to the material while the sintered part is exposed to the contaminated oxidized surface [37]. A second small peek is seen forming around 2θ 38.8º from the continuation of high temperature exposure made the part into a crystalline layer of cupric oxide (CuO) at the cost of a cuprous oxide (Cu_2O) phase [38].

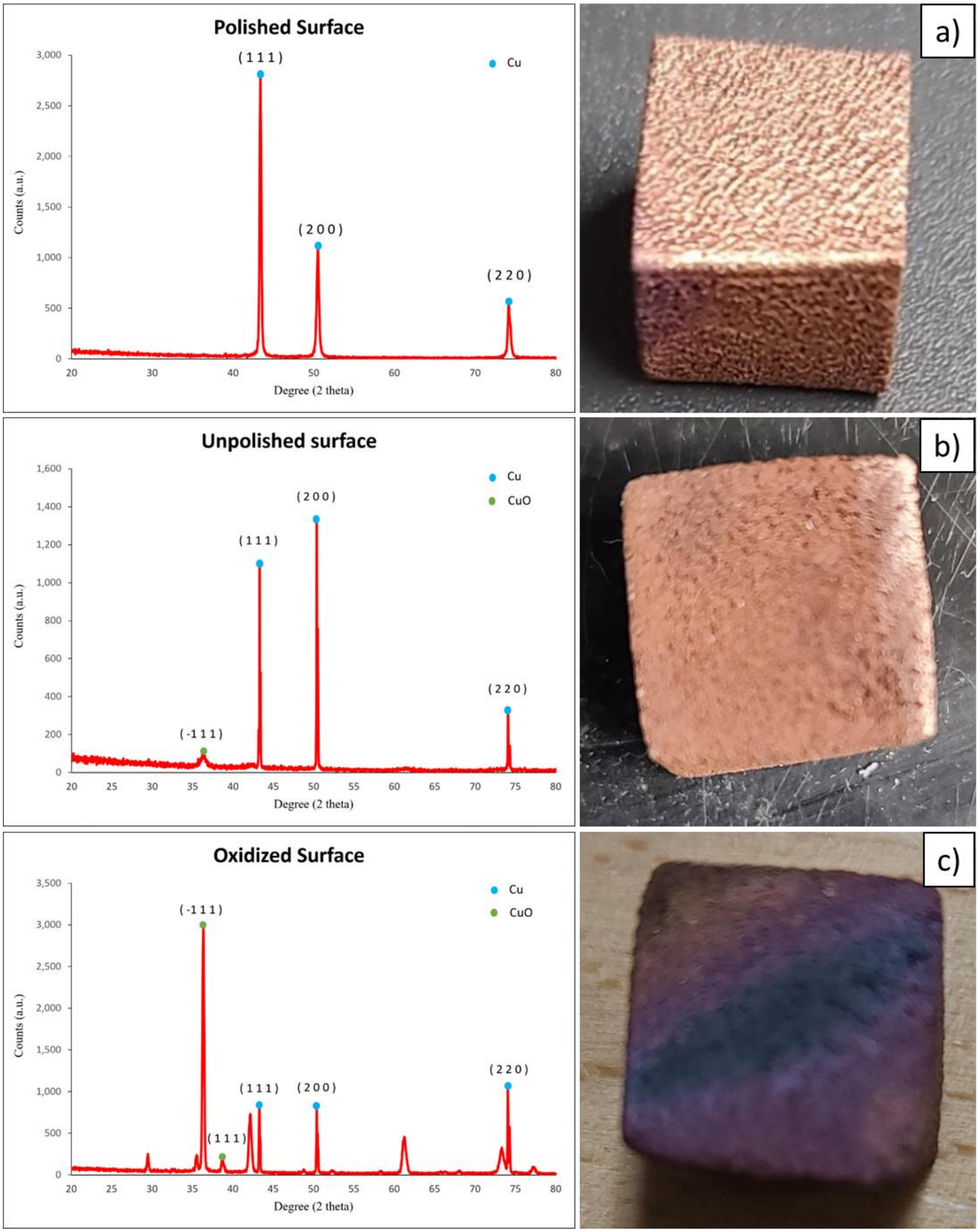

Figure 1.11. XRD patterns of 3D printed sintered parts showing different faces. Polished (a), unpolished (b), and oxidized surfaces (c).

Section 1.4.5. Geometry analysis and distortion compensation

Distortion compensation in FFF (Fused Filament Fabrication) is a process used to counteract the warping or deformation that occurs during the printing of parts using FFF technology. This is due to the cooling and contraction of the melted plastic material as it is deposited layer by layer [39]. However, in this study, the FFF printed parts are subjected to sintering due to the composite characteristics of the material, only the metal component, copper, is desired from the filament used for printing. Parts are subjected to de-binding and sintering processes to eliminate the polymer component and achieve the optimal properties of copper; this distortion compensation is used to reduced shrinkage and warping from the post-processing procedures such as in the case for Binder Jetting. Borujen et al. developed an algorithm that compensates for sintering deformations and shrinkage for binder jetting sintered parts with a 3% tolerance level. The team analyzed the deformation and shrinkage of five different geometries: cube, window, reverse-U, frame, and Z structure. The study considered factors such as densification, gravity, friction, and buckling of walls [40]. In contrast, our study presents a methodology to minimize shrinkage and warping deformations in MF3 sintered parts by using inverse pre-distortion from 3D scanned sintered reverse U parts.

Finally, our study provides a detailed exploration of shrinkage and distortion in MF3 sintered parts. Figure 1.12. provides a visual comparison of the original green part, the sintered part, and three iterations of the reverse compensation process. Each iteration aimed to reduce the deviation from the original digital file caused by sintering deformations and shrinkage. The comparison helps to illustrate the effectiveness of the methodology in minimizing deformation and shrinkage in the sintered parts. The iterations were repeated until the deviation percentage was within an acceptable range of less than 6%.

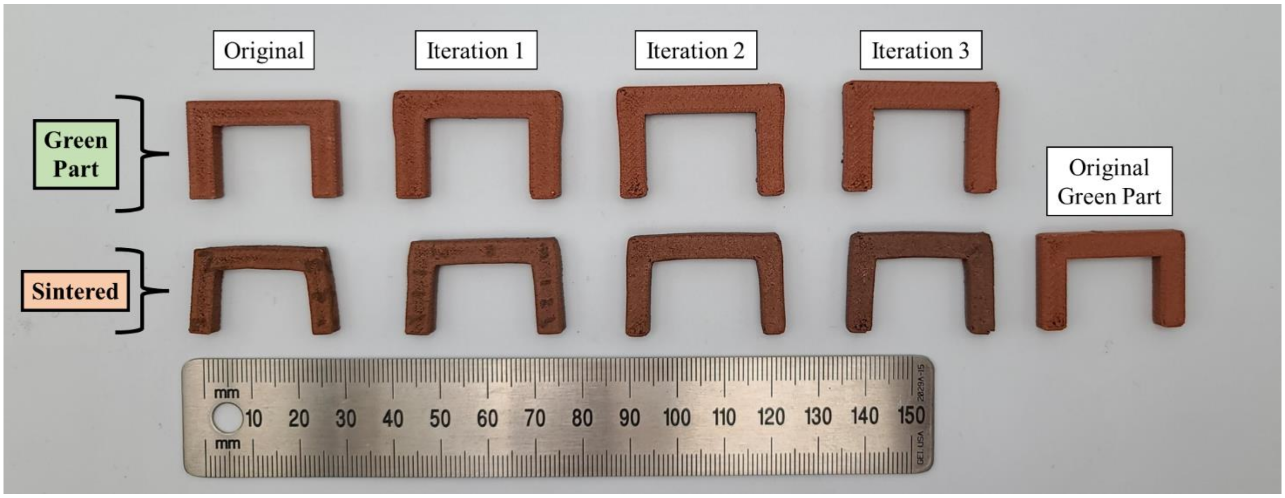

Figure 1.12. Inverse pre-distortion model iteration process results from original to iteration 3.

The gradient in Figure 1.13. represents the deviation in mm of the part compared to the digital file. The red gradient indicates an increase in distance or deformation, while the blue gradient represents negative values for shrinkage. Figure 1.13.a illustrates that the printed green part has already deviated from the digital file with an increase in distance. Figure 1.13.b demonstrates that the deviation has changed from an increase to a decrease due to shrinkage that happened from the sintering process. In Figure 1.13.c, the first iteration of the process resulted in an overall deviation of 1.39 mm increase and -1.32 mm decrease. In Figure 1.13.d, the second iteration showed an increase of 1.72 mm and a decrease of -2.39 mm. These changes can be attributed to a reduction in part deformation and warping, as well as the implementation of the new pre-distorted part. It is possible that the pre-distorted part had more defects compared to the previous iteration print, which could have contributed to the observed deviations. However, overall, these changes resulted in less shrinkage in the print-head direction. Finally, the deviation was reduced by reverse compensating the distance in the print-head direction in the pre-distortion model, resulting in an increase of 0.81 mm and a shrinkage of -0.68 in Figure 1.13.e. This optimization was achieved by carefully adjusting the pre-distortion model, particularly in the print-head direction, to reduce deformation and warping in the part.

To gain a better understanding of deviation in each printing orientation, a comprehensive study was conducted. All iterations were digitally scanned and analyzed with GOM inspect. Multiple points were created per printing orientation with the deviation label tool, and areas were selected where the most severe deformations or distances were observed. Then, the data were exported to a CSV file, averaged, and statistically analyzed in Excel. Figure 1.14. shows the geometry deviation comparison from the original CAD in all three printing orientations (i.e. print-head, print-bed, and build directions). The deviation analysis of the original green part revealed high deviation values of 3.34%, 21.89%, and 6.16% in the print-head, build, and print-bed directions, respectively. These values indicate that significant deviation was already present in the green part before sintering. After sintering, the deviation values shifted towards shrinkage, resulting in values of -8.54%, -25.94%, and -9.71%, respectively, which is typical for sintered parts. The first pre-distortion iteration substantially reduced the deviation values, with -5.43%, -5.88%, and 2.39% for the print-head, build, and print-bed directions, respectively. However, in the second iteration, the deviation values fluctuated, and the only improvement achieved was a reduction of -3.74% in the build direction, while the deviation increased for the print-head and print-bed directions by -6.76% and 2.51%, respectively. The third and final iteration of the pre-distortion process significantly minimized the deviation percentage in the print-head and print-bed directions to 1.82% and 1.50%, respectively, while increasing the deviation in the build direction to 5.28%. This increase in the build direction deviation can be attributed to the interlayer gaps created during the printing process [40].

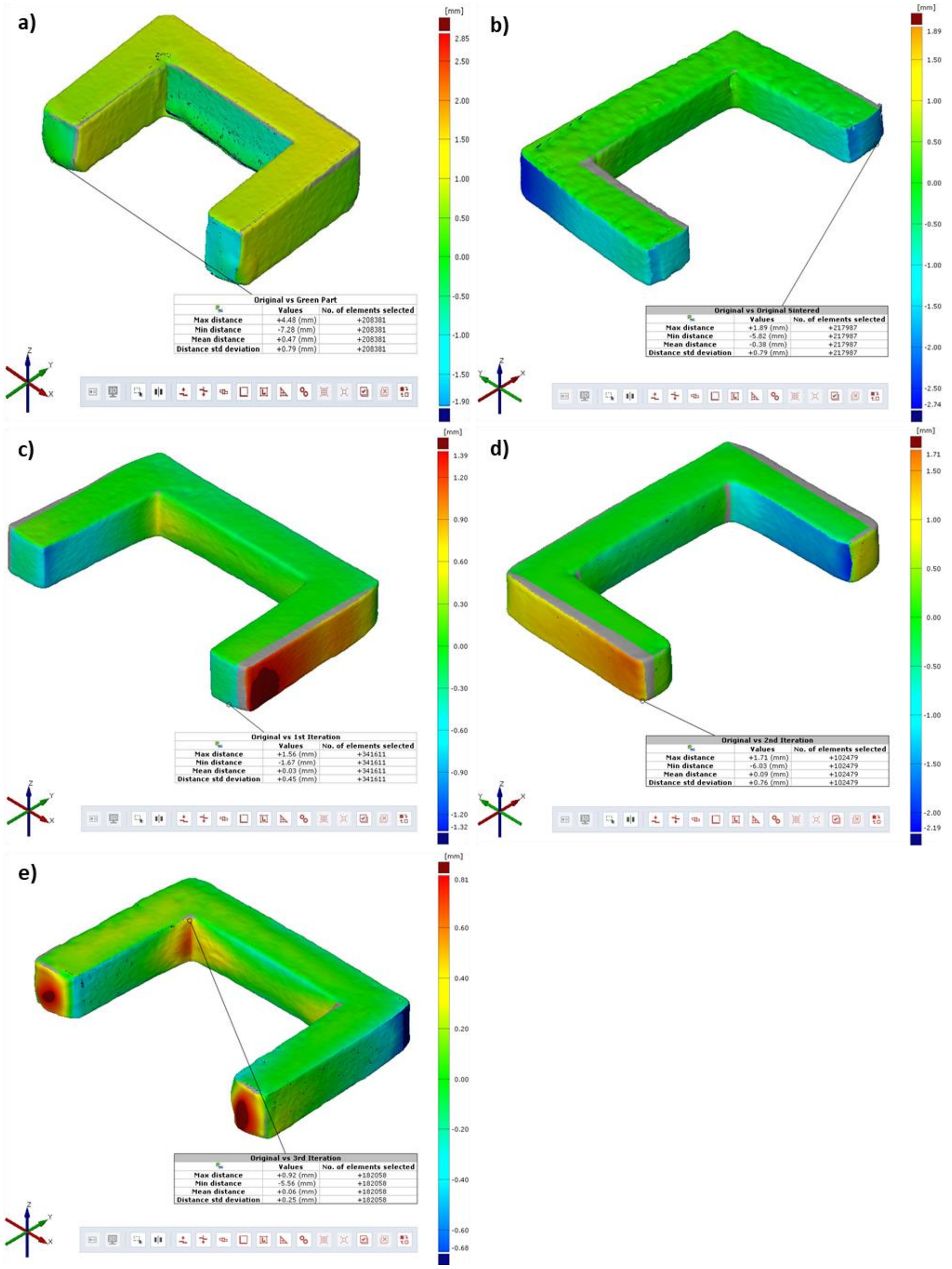

Original vs Green Part

	Values	No. of elements selected
Max distance	+4.48 (mm)	+208381
Min distance	-7.28 (mm)	+208381
Mean distance	+0.47 (mm)	+208381
Distance std deviation	+0.79 (mm)	+208381

Original vs Original Sintered

	Values	No. of elements selected
Max distance	+1.89 (mm)	+217987
Min distance	-5.82 (mm)	+217987
Mean distance	-0.38 (mm)	+217987
Distance std deviation	+0.79 (mm)	+217987

Original vs 1st Iteration

	Values	No. of elements selected
Max distance	+1.56 (mm)	+341611
Min distance	-1.67 (mm)	+341611
Mean distance	+0.03 (mm)	+341611
Distance std deviation	+0.45 (mm)	+341611

Original vs 2nd Iteration

	Values	No. of elements selected
Max distance	+1.71 (mm)	+102479
Min distance	-6.03 (mm)	+102479
Mean distance	+0.09 (mm)	+102479
Distance std deviation	+0.76 (mm)	+102479

Original vs 3rd Iteration

	Values	No. of elements selected
Max distance	+0.92 (mm)	+182058
Min distance	-5.56 (mm)	+182058
Mean distance	+0.06 (mm)	+182058
Distance std deviation	+0.25 (mm)	+182058

Figure 1.13. Maximum/minimum distance, mean, and standard deviation of reverse U Original stl vs scanned sintered part. Original vs green part [ISO Standard view X+ Y- Z+] (a), original vs original sintered part [ISO Standard view X- Y- Z+] (b), original vs first iteration [ISO Standard view X+ Y- Z+] (c), original vs second iteration [ISO Standard view X- Y- Z+] (d), and original vs third iteration [ISO Standard view X+ Y- Z+] (e).

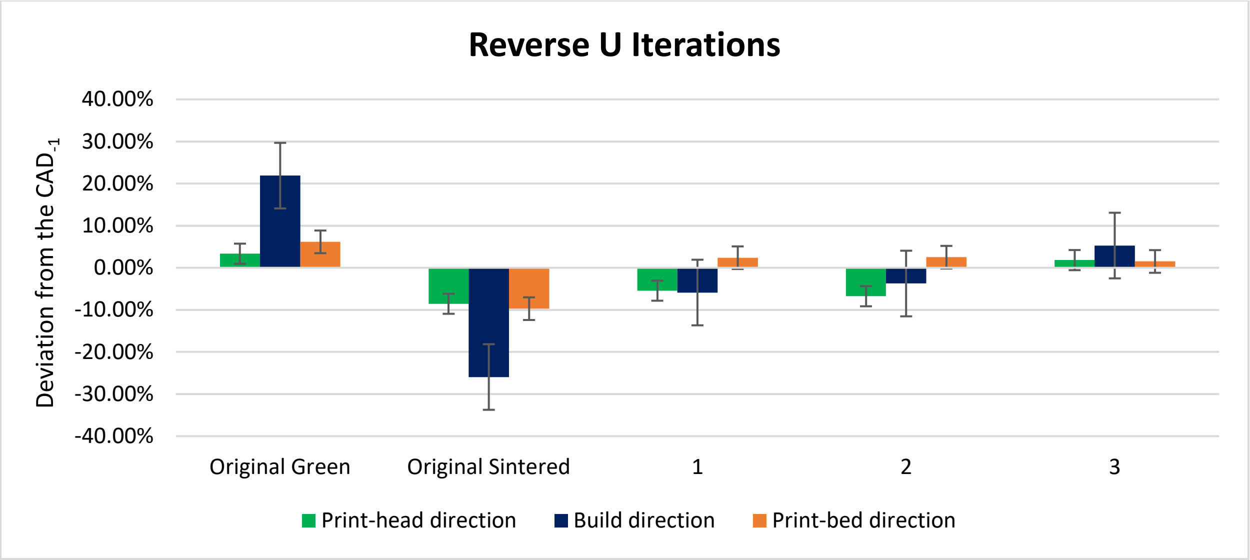

Figure 1.14. Deviation percentage of compared by iteration from the reverse U STL.

Section 1.5. Conclusion

Based on the experimental and statistical results presented in this study, several conclusions can be drawn:

- Overall, the sintered parts achieved densities ranging from 7.65 to 8.03 g/cm3, which are consistent with dense sintered copper parts.
- Particle diameter was measured which ranged from 22.55 um to 71.2 um.
- The pore size diameter recorded ranged from 5.42 um to 21.21 um with an average pore size diameter of 15.44 um.
- The total average pore area relative to the entire microstructure is 18.12%.
- The total average grain size obtained was 50.76 µm.
- The XRD results show crystallinity peaks of Cu in 2θ 43, 50, and 74° which represent (111), (200), and (220) for crystalline orientations respectively and are standard for Cu results that are sintered.

- CAD vs the iteration showed a deviation of 1.82%, 5.28%, and 1.50% for the print-head direction, build direction, and print-bed direction, respectively.

Our findings show that deformation and shrinkage of MF3 sintered parts can be controlled by 3D scanning, comparing to the digital model, creating a reverse deformation compensated part. Moreover, we employed sacrificial carbon during sintering to shield the printed part from oxidation, which has proven to be an effective method for reducing post-processing costs.

Chapter II: Electrochemical Conversion of Pollutants to Value-Added Products Using 3D Printed Metal Fused Filament Fabrication (MF3) Parts

Section 2.1. Abstract

Metal fused filament fabrication (MF3) is a rapidly growing additive manufacturing technology that enables the creation of complex metal parts with high accuracy and precision. Copper, a highly conductive metal with various applications in industries such as electronics and aerospace, is a promising material for MF3. In this study, we investigated the use of MF3 copper parts to fabricate copper electrodes for CO2 electrochemical reduction. We examined the post-processing manufacturing process of debinding and sintering to obtain fully 3D printed copper parts in an air environment. Our results demonstrate that MF3 copper parts have high porosity, providing a larger active surface area that is suitable for nitrate reduction and results in the production of ammonia. These findings hold great potential for the use of copper in additive manufacturing and other advanced manufacturing applications.

Section 2.2. Introduction

Fused Filament Fabrication (FFF) is an additive manufacturing method that uses a heated nozzle to extrude thermoplastic filament, melting it briefly before depositing it layer by layer to form a green part. FFF is a popular technology because it is affordable, allows for quick processing, minimizes material wastage, has a user-friendly interface, allows for precise control of processing parameters, can create intricate components, and can work with a range of materials [1] [2] [3]. Although Fused Filament Fabrication (FFF) is a cost-effective additive manufacturing process, it has limited applications for producing functional parts on a global scale. This is due to several factors such as poor part properties, limited raw material selection, low printing temperature, size restrictions, and low production rates. These limitations can impact the overall quality, complexity, and scalability of the parts being produced. Despite these challenges, FFF remains a popular choice for rapid prototyping and small-scale production in certain industries. There are ongoing efforts to address these limitations and expand the potential applications of FFF in the future [4]. New materials are currently under development to overcome the limitations of FFF technology. This includes Metal Fused Filament Fabrication (MF3) technology, which allows for the fabrication of metal and ceramic components [4].

The MF3 technique is an innovative approach that uses a combination of thermoplastic binder and metal powder to create a composite metal filament suitable for 3D printing using FFF. This technique allows for the creation of various metal objects such as Inconel, titanium, bronze, stainless steel, aluminum, copper, and other metals using commercially available polymeric filaments blended with metallic powders. This approach has made it affordable and convenient to produce 3D metal objects using readily available 3D printers [5]. Metal additive manufacturing techniques, such as Powder Bed Fusion (PBF), Direct Metal Sintering (DMLS), Electron Beam Melting, Binder Jetting (BJ), and Selective Laser Melting (SLM), offer a wide range of material selection and superior mechanical properties. However, they are challenging to implement and expensive due to their high-energy processes, strict powder property requirements for printability, and the need for atmospheric controls to prevent oxidation [2] [7] [8], [9]. Compared to other metal additive manufacturing techniques, MF3 offers several advantages such as low cost, non-toxic materials, user-friendly interface, and low maintenance requirements [2] [10]. Making this technology useful where high mechanical properties are not the focus. It is well-known that additive manufacturing is highly dependent on the specific application and is not suitable for all manufacturing needs. Therefore, we utilized MF3 copper to produce cost-effective electrodes with high porosity suitable for CO2 electrochemical reduction, with copper acting as the catalyst.

In recent years, researchers have explored the use of FFF for electrochemical reduction, which involves converting a pollutant like carbon dioxide into valuable products such as methane, ethylene, and methanol, by using conductive composites to generate 3D-printed electrodes for energy storage and electrochemical analysis [41] [42]. Copper is a highly conductive metal that has been identified as a promising catalyst for CO2 or nitrate electrochemical reduction. In this context, the use of MF3 copper electrodes to evaluate the efficiency and selectivity of copper as a catalyst for CO2 or nitrate electrochemical reduction has attracted significant interest. The advantages of MF3 technology include its low cost, ease of use, and capacity to produce parts with high porosity, which provides a higher active surface area suitable for CO2, or nitrate electrochemical reduction.

Carbon dioxide (CO_2) electrochemical reduction is a promising method for converting CO_2 emissions into valuable chemicals and fuels. This technology has the potential to not only reduce greenhouse gas emissions but also provide a sustainable source of feedstocks for the chemical industry. As countries around the world work to meet their emissions reduction targets and transition to a low-carbon economy, CO2 electrochemical reduction technology could play a significant role in supporting global economic growth [43] [44]. Currently, 36.8 billion metric tons are being generated annually in 2022 [43]. Furthermore, as the demand for renewable energy sources increases, the development of this technology could drive the growth of a new industry, creating jobs and economic opportunities [45]. In addition, ammonia is also a highly valuable chemical product that is very important in energy/industrial applications with an annual production of 175 million metric tons reported in 2019 [46]. In this study, we will be assessing the sintering process of MF3 3D printed parts under air environment conditions by using sacrificial carbon to shield the part against oxidation while also evaluating the electrochemical reduction of CO_2, nitrate, and reversible hydrogen electrode (HER) reactions.

Section 2.3. Materials and Methods

Section 2.3.1. Materials and equipment

The copper filament (The Virtual Foundary, Stoughton, WI) used in this study has a diameter of 1.75 mm in a 1kg spool which contains 87.0% - 90.7% metal with a density of 4.8 g/cc - 5.0 g/cc. The 3D printer used to fabricate the parts was from Creality CR5-PRO High Temperature model (Creality 3D Technology Co, SZ, CHN) with a print volume of 300x225x380mm. Max build plate and nozzle temperature are 110 °C and 300 °C respectively. The debinding and sintering process was carried out using Deltech Furnace DT-31-FL-8-E3504 Front Load Furnace (Deltech Furnaces, USA) and sacrificial carbon (The Virtual Foundary, Stoughton, WI) to shield the part from oxidation. The debinding process was performed at air environment conditions at a ramp rate of 1 °C/min and dwell time of 4 hours at 482 °C. The sintering schedule was conducted at air environment at a ramp rate of 2 °C/min and dwell time of 5 hours at 1052 °C.

Section 2.3.2. Electrochemical measurements

The electrochemical measurements were performed using potentiostat SP-150e from Bio-logic (Seyssinet-Pariset, France), in an H-type electrochemical cell. The working electrode in this study was a copper MF3 electrode, while a platinum wire served as the counter electrode, and a commercial mercury/mercury oxide acted as the reference electrode. The 3D printing and debinding/sintering process were utilized to control the active surface area exposed. The cathode and anode compartments were each filled with a specific solution to facilitate either CO2 reduction or nitrate reduction. For CO2 reduction, a 0.5M solution of potassium bicarbonate (KHCO3) was added to both compartments, and CO2 gas was purged for 30 minutes. Nitrate reduction was facilitated by a solution of 1M sodium hydroxide (NaOH) and 0.1M sodium nitrate (NaNO3), which was added to both compartments, and N2 gas was purged for 30 minutes. Measurements of all potentials were referenced to the reversible hydrogen electrode (RHE). Cyclic voltammetry (CV) was performed using a scan rate of 10 mV/s and Linear Sweep Voltammetry (LSV) was performed using a scan rate of 2 mV/s. Following the voltametric experiments, the current density was determined at a specific potential, which corresponded to the midpoint potential in either the positive or negative sweep of the cyclic voltammogram.

Section 2.3.3. Part fabrication

Mf3 parts were designed using Fusion 360 (Autodesk, USA) and sliced using Ultimaker Cura version 4.11.0 (Ultimaker B.V., USA) 3D slicer software. The printing parameters used can be found in table 2.1. In addition, printed parts were printed at several gyroid infill densities ranging from 10% to 100% infill densities. The gyroid infill pattern was selected for its ability to generate internal porosity, which varies based on the infill percentage. For the copper electrode, a 60% infill percentage was chosen to ensure structural integrity and to maximize the exposed surface area, which is critical for the electrochemical reduction reaction. The printed parts were then post-processed through debinding and sintering. The complete fabrication process can be observed in Figure 2.1.

Table 2.1. Printing parameters

Nozzle temperature	Bed temperature	First layer height	Layer height	Nozzle speed	First layer extrusion width percentage
247 °C	80 °C	0.12 mm	0.2 mm	40 m/s	125 %

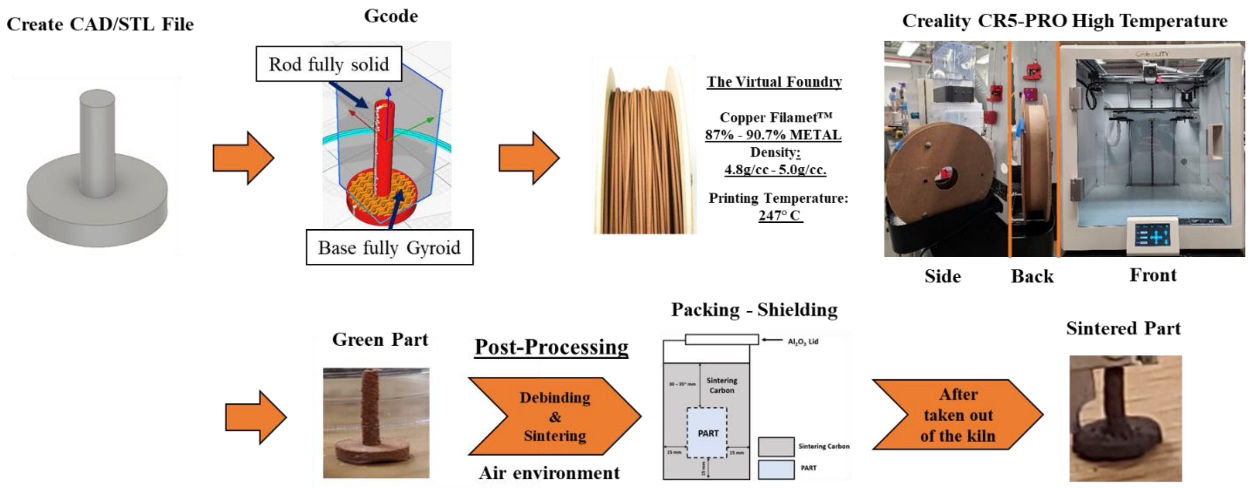

Figure 2.1. MF3 manufacturing process schematic for copper electrode.

Section 2.3.4. Debinding

The debinding packing process was carried out by placing the printed parts in a Al2O3 crucible, depositing sacrificial carbon (The Virtual Foundary, Stoughton, WI) inside the crucible, and allocating a lid on top of the crucible while leaving an opening as seen in figure 2.2. The sacrificial carbon was added to shield the green printed part from oxidation in air environment and the Al2O3 lid was used to limit the consumption of carbon during the process. As mentioned, the debinding schedule parameters were ramp rate, target temperature, and dwell time being 1 °C/min, 482 °C, and 4 hours respectively. The debinding process allows the binder material to exit the part by heat. Any residual binder material can be later removed during the sintering process.

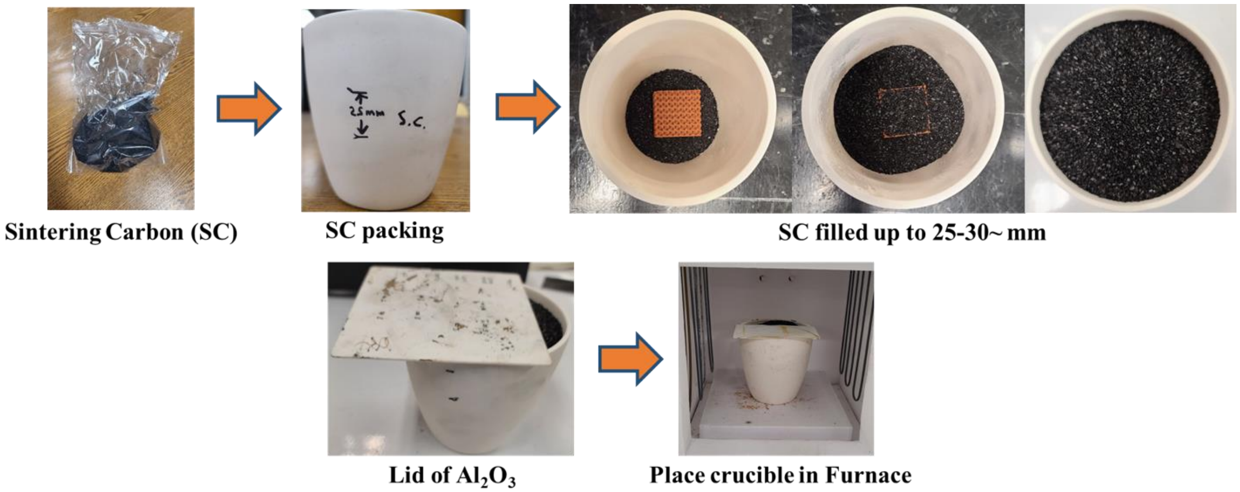

Figure 2.2. MF3 debinding packing schematic.

Section 2.3.5. Sintering

The debound parts were then sintered using a ramp rate of 2 °C/min, target temperature of 1052 °C, and a dwell time of 5 hours. The sintered parts were then cooled to room temperature in air environment conditions. The sintering packing process was performed identically to the debinding packing process.

Section 2.3.6. nTopology

Structures that prioritize a high surface area are best suited to optimize the reduction of nitrates and CO2. Thus, triply periodic minimal surface (TPMS) structures were identified as a prime candidate for this purpose. TPMS structures are defined by trigonometric functions, and result in zero mean curvature with a high surface area [47]. Many TPMS structures exist, but the gyroid function was utilized due to the high surface area coupled with the macropores of the lattice. TPMS structures have been shown to optimize piezoelectric properties [48], mechanical properties [49] and thermal properties [50]. To generate the TPMS structure, a commercial software known as nTopology (New York, USA) was employed. This software enables efficient and streamlined generation of complex structures. To generate the novel gyroid cube, a 32 mm^3 was created. Next, the TPMS block was used to generate the TPMS structure. To prioritize the macro pores, the mid-surface offset was altered, resulting in a structure with a minimum feature size of 0.74 mm. Lastly, the structure was given a base through a Boolean union, meshed, and exported as a STL file. The structure may be seen below in Figure 2.3., without its base. The TPMS gyroid lattice was later 3D printed and sintered.

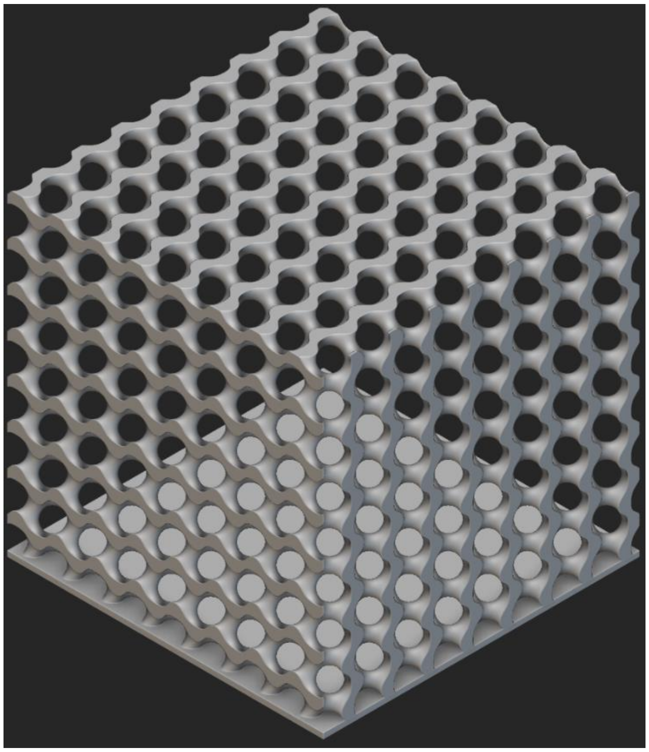

Figure 2.3. Implicit body of Offset TPMS structure

Section 2.3.7. Characterization

Various characterization techniques were utilized to investigate the density, grain size, microstructure, and composition of the sintered components. These techniques encompassed Gravimetric analysis, Optical Microscopy, Scanning Electron Microscopy (SEM), and X-Ray Diffraction (XRD).

Section 2.3.7.1. Density analysis

The density of the sintered specimens was determined using an Archimedes principle-based apparatus equipped with a TDK03 kit and a Sartorius model QUINTIX613-1S (Thermo Fisher Scientific, Waltham, MA, USA). The weight of the part in air and water was measured in accordance with ASTM Standard B962-15 [21]. All sintered samples underwent the same heating schedule and debinding process.

Section 2.3.7.2. X-Ray Diffraction

To evaluate the effectiveness of sintering carbon for shielding purposes, X-ray diffraction (XRD) analysis was conducted on the sintered copper part. The analysis was carried out utilizing a DISCOVER diffractometer (Bruker, Boston, MA, USA) with CuKα radiation.

Section 2.3.7.3. Digital Optical Microscope

Digital imaging was utilized to obtain optical microscopic images using a VFX-970F Keyence Digital Microscope (Keyence, Itasca, IL, USA). The samples were examined at magnifications ranging from 20-500X, and the porosity area was measured using the Keyence measuring tool.

Section 2.3.7.4. Scanning Electron Microscope

Scanning Electron Microscope (SEM) was utilized to obtain microscopic images using a Phenom ProX desktop SEM (Thermo Fisher Scientific, Achtseweg Noord 5, 5651 GG Eindhoven, The Netherlands). The SEM micrographs of sintered structures with different gyroid infill percentages were examined, and the microstructure was evaluated to check interparticle bonding.

Section 2.4. Results and discussion

Section 2.4.1. Density analysis

The gravimetric analysis was conducted to evaluate the efficiency of the sintering process. Green 3D printed parts with different infill percentages were later sintered and analyzed as seen in Figure 2.4. and 2.5. Different infills percentages were evaluated to maximize active surface area for the 3D sintered parts. The different infill percentages of the green parts are shown in Figure 2.4. Infill percentages ranging from 10 to 50% were put in a crucible and were sintered together. 60 to 100% were sintered together in a different crucible. Different shapes were used to identify the sintered parts after the sintering process. The 10 to 30% infill percentages were fragile specimens after sintering and their partial broken structure can be seen in Figure 2.5. In addition, polishing was performed on these specimens to remove any remaining impurities from the surface. The results showed that the sintered parts had an average density of [6.95 g/cm3] which is lower than traditionally manufactured copper at room temperature with a density of 8.96 g/cm^3 [22]. In Figure 2.6., densities ranging from 80 to 100% infill show a decrease in density. This can be attributed to the printing process, where gaps can be created between the interconnect layers where the material is deposited, resulting in defects and voids that contribute to lower density. Similarly, the debinding process creates interconnected channels as the binder material degrades and exits the part, leading to voids and a decrease in part density [23]. Nevertheless, the amount of porosity induced due to the infill percentage used and the printing/debinding/sintering process can translate to higher surface area exposed. This indicates that the sintering process was effective to fabricate semi-dense copper parts, which can increase the reaction rate and efficiency for the electrochemical reduction of CO_2 and nitrate [51] [52].

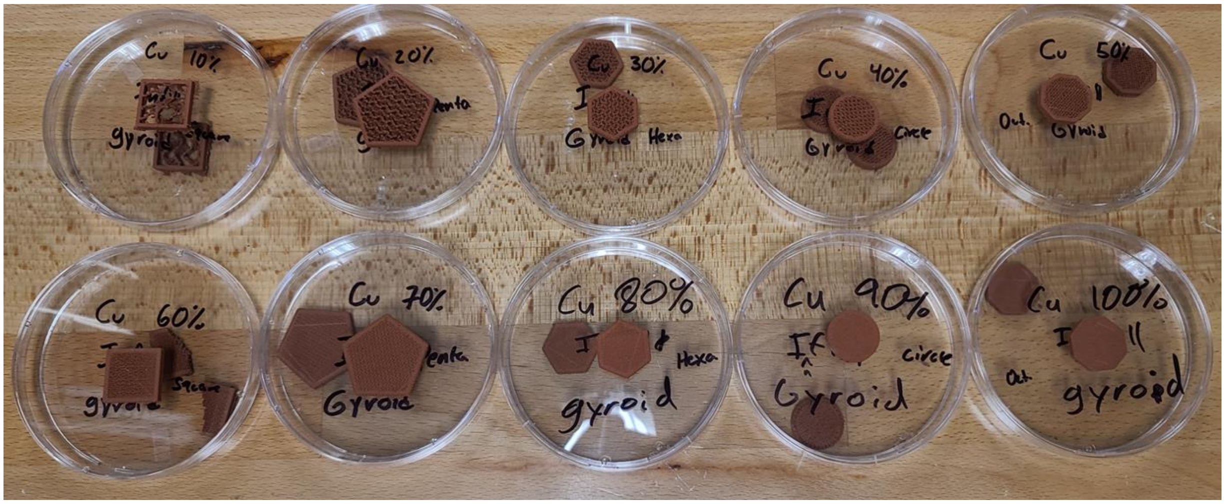

Figure 2.4. Different green structures ranging from 10-100% gyroid infill percentage.

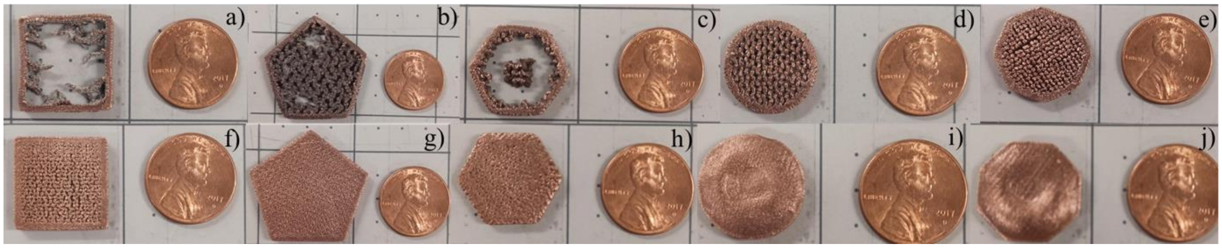

Figure 2.5. Different sintered structures ranging from 10-100% gyroid infill percentage. 10% (a), 20% (b), 30% (c), 40% (d), 50% (e), 60% (f), 70% (g), 80% (h), 90% (i), and 100% (j).

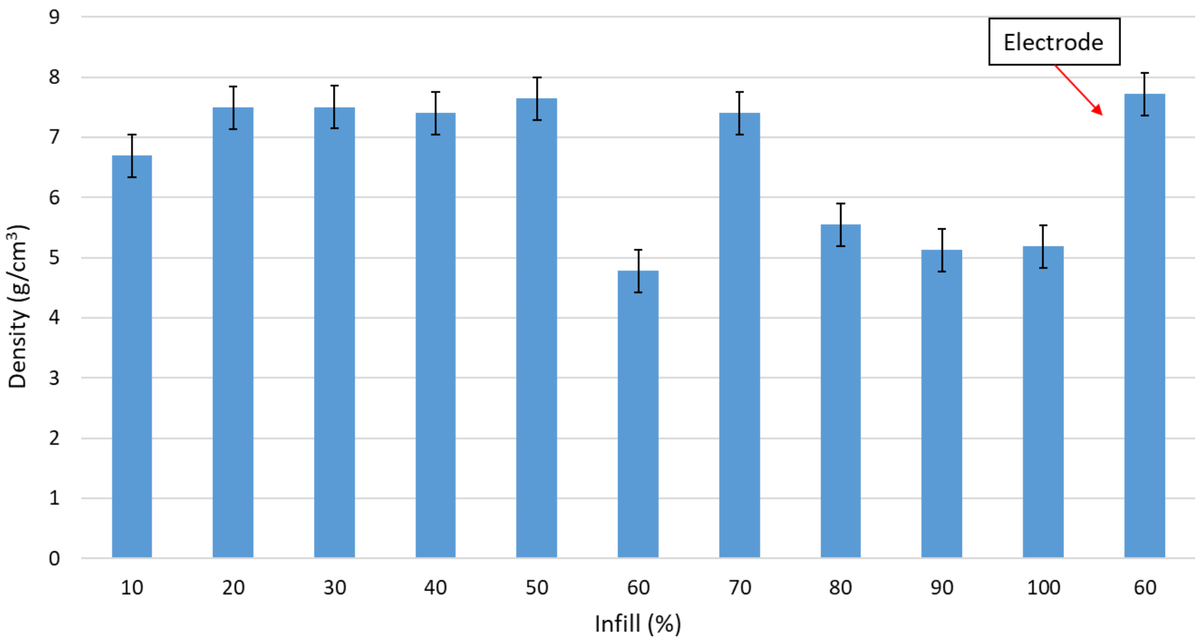

Figure 2.6. Density of the sintered infill percentages and electrode density.

Section 2.4.2. X-Ray Diffraction

The XRD analysis was conducted to evaluate the crystallographic structure of the sintered parts. The XRD pattern showed diffraction peaks corresponding to the crystallographic planes of the metal used in the printing process as seen in figure 2.7. Results show Bragg reflection angles at 2θ of 43°, 50°, and 74° and crystal orientations of (111), (200), and (220) respectively [53]. The absence of any other phases or impurities in the XRD pattern indicated that the sintering process was successful in producing a pure metal microstructure. These characteristic peaks confirm face-centered cubic (FCC) copper phase without oxidation or other impurity phases during sintering [54]. This analysis proves that using sacrificial carbon is an effective method to fabricate these MF3 copper parts in air environment with no indication impurities or crystallinity phase changes.

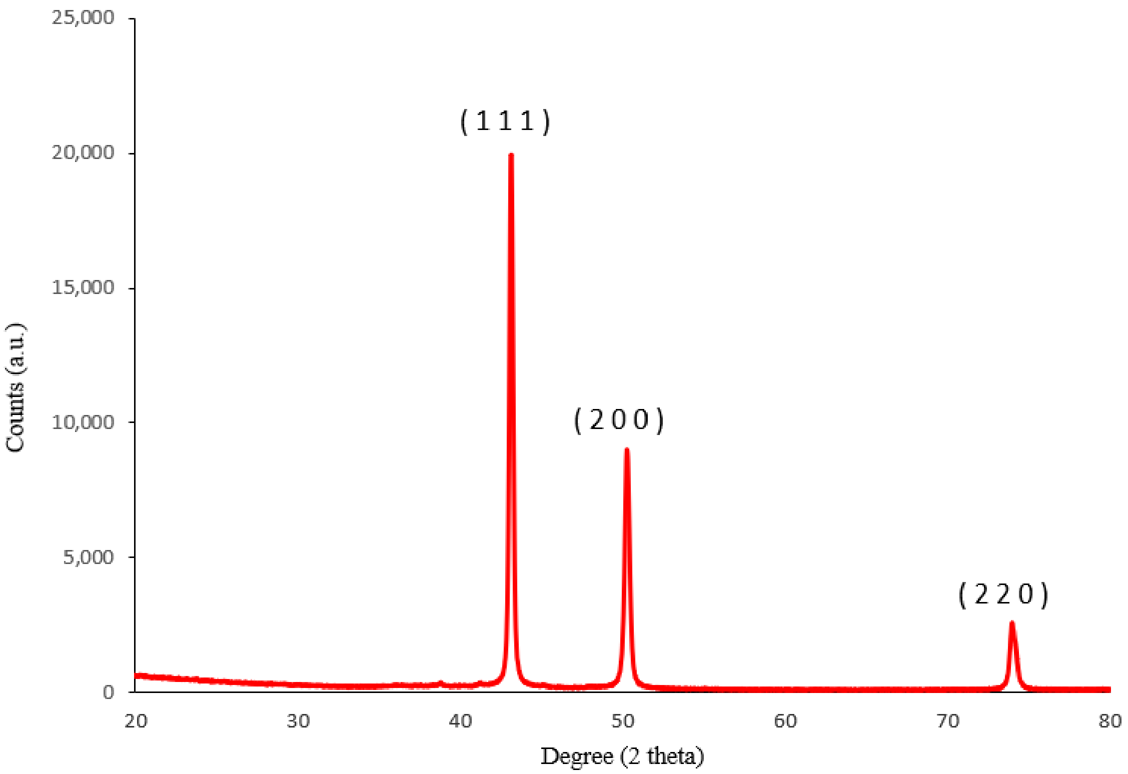

Figure 2.7. XRD patterns of sintered copper.

Section 2.4.3. Digital Optical Microscope

Figure 2.8. shows the microstructure of a sintered part which followed the same sintering schedule as the copper electrodes. Pore areas were measured and a table with average pore size can be seen in table 2.2. As previously mentioned, the porosity of this sample was induced by the printing parameters, debinding, and sintering schedules. The average pore size diameter found in the sintered part was 48.9 µm. Furthermore, the observed pore size is similar to that achieved in another study by Mohammad Qasim Shaikh, who used the MF3 method with 59 volume % of Ti-6Al-4V, where they achieved an average pore size diameter of approximately 50 µm [55]. Yet, porosity in MF3 sintered parts is highly dependent on the debinding and sintering schedule. A low ramp rate during debinding allows the binder material to heat, melt, degrade, and evaporate, relieving internal pressure and resulting in lower porosity and deformation. Similarly, a lower ramp

rate during sintering can also contribute to densification of the part [23]. In Figure 2.9., a cross-section of the sintered part can be examined. The cross-section was obtained using a diamond blade, but due to the friction and melting during the cutting process, most of the cross-section was lost, giving the appearance of a polished surface.

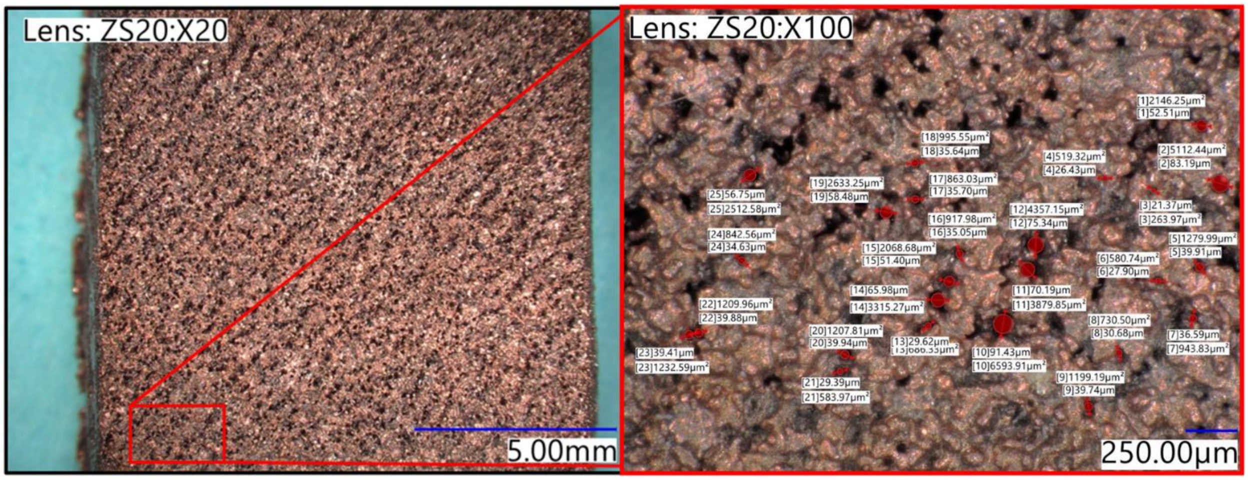

Figure 2.8. Digital optical microscope image at 20-100X magnification of sintered part.

Table 2.2. Sintered part pore size diameter and area analysis of Figure 3.7.

Pore Number	Pore Diameter (µm)	Pore Area (µm^2)	Pore Number	Pore Diameter (µm)	Pore Area (µm^2)
1	52.51	2146.25	14	65.98	3315.27
2	83.19	5112.44	15	51.4	2068.68
3	21.37	263.97	16	35.05	917.98
4	26.43	519.32	17	35.7	863.03
5	39.91	1279.99	18	35.64	995.55
6	27.9	580.74	19	58.48	2633.25
7	36.59	943.83	20	39.94	1207.81
8	30.68	730.5	21	29.39	583.97
9	39.74	1199.19	22	39.88	1209.96
10	91.43	6593.91	23	39.41	1232.59
11	70.19	3879.85	24	34.63	842.56
12	75.34	4357.15	25	56.75	2512.58
13	29.62	686.33	Average	45.89	1867.1

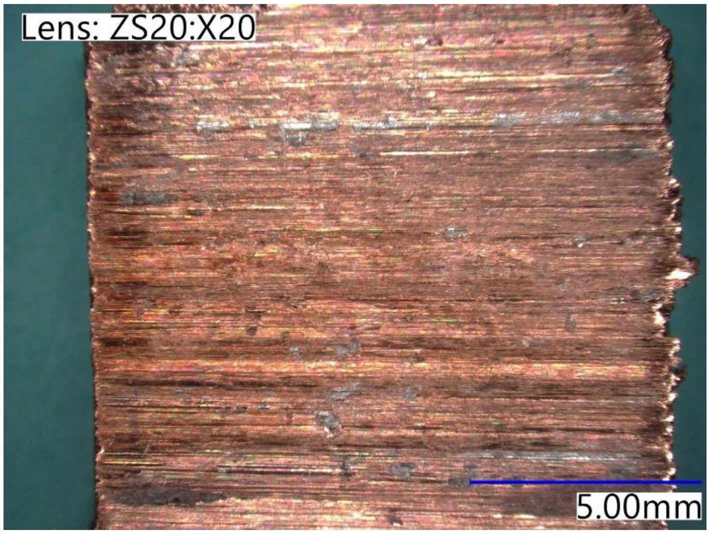

Figure 2.9. Digital optical microscope image at 20X magnification of a cross-section of the sintered part.

Figure 2.10. shows the pore size analysis of a sintered part with 60% infill, with corresponding data presented in Figure 2.12. The measured pore size ranged from 7 to 22.5 um. Figure 2.11. illustrates the microstructure and porosity, and the corresponding data is shown in Figure 2.13., with pore sizes ranging from 7.5 to 21 um. The pore length of the copper sintered electrode with 60% infill was evaluated in Figure 2.14, with the void length ranging from 0.2 to 0.64 mm. These findings suggest that the porosity in our sintered parts is consistent and independent of the infill percentage of the printed part. All sintered parts underwent debinding and sintering at the same temperatures, and ramp rates, therefore having the same pore size diameter.

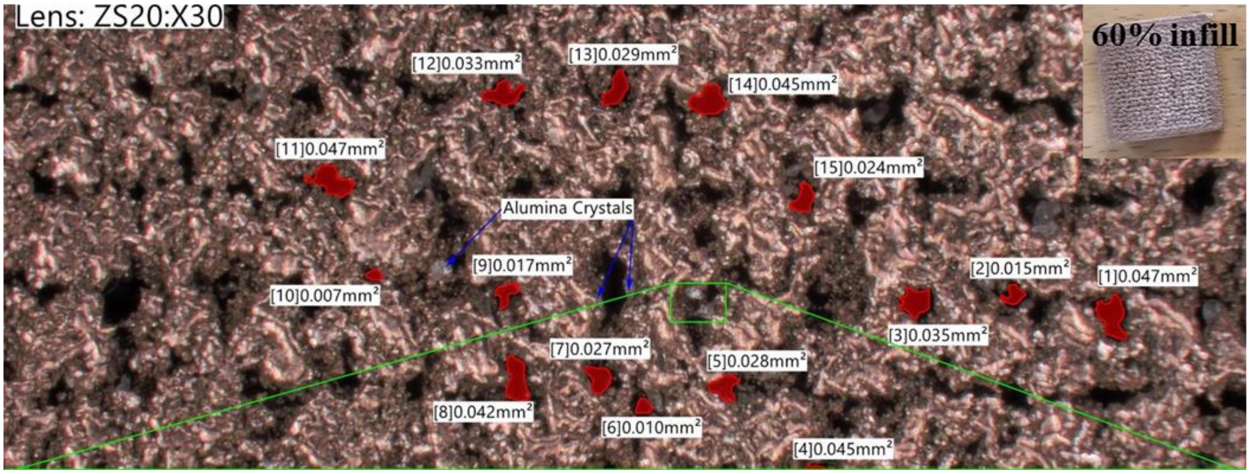

Figure 2.10. Digital optical microscope image at 20-200X magnification of sintered part with 60% infill.

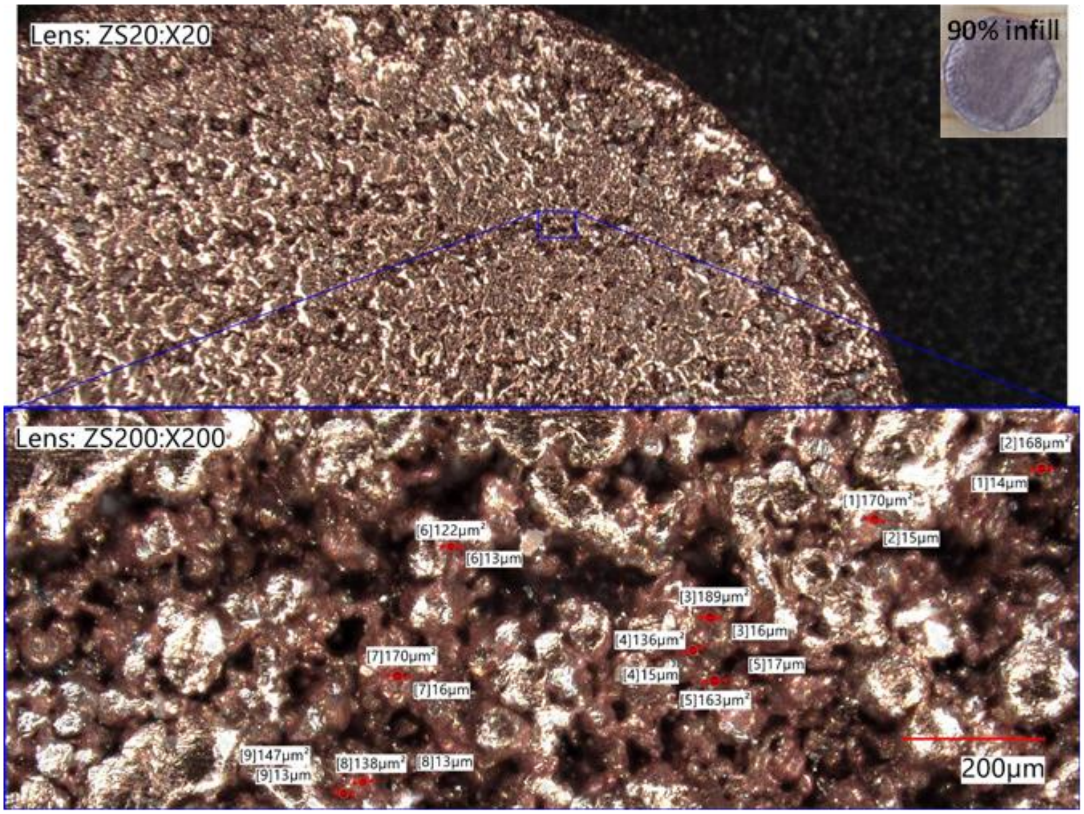

Figure 2.11. Digital optical microscope image at 20-200X magnification of sintered part with 90% infill.

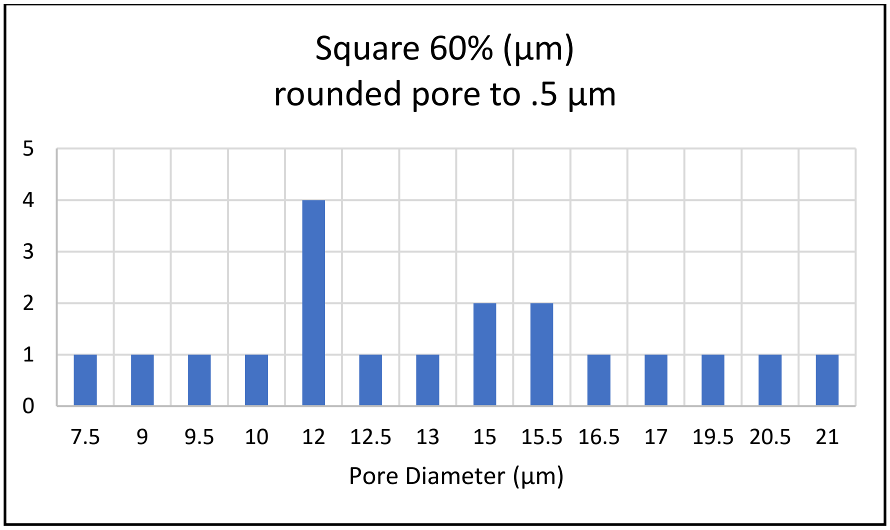

Figure 2.12. Pore size diameter analysis of sintered part with 60% infill.

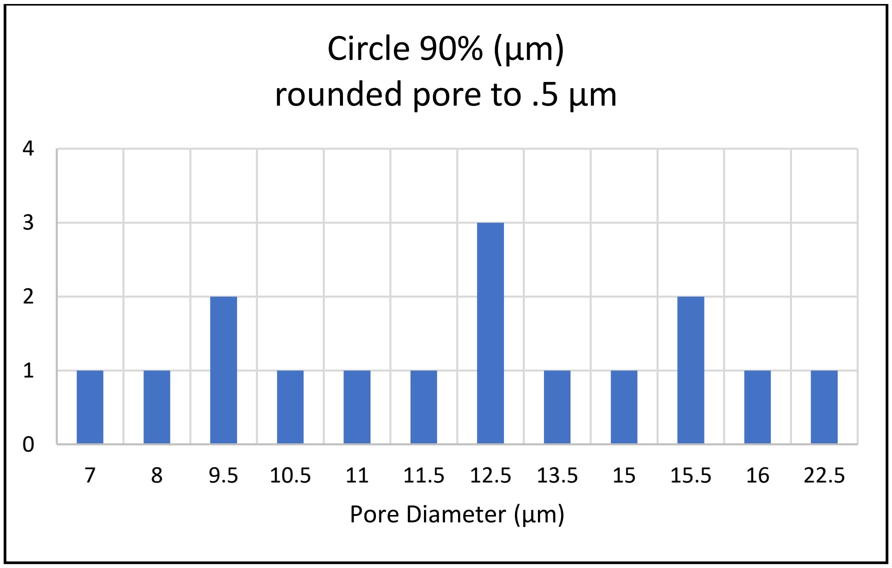

Figure 2.13. Pore size diameter analysis of sintered part with 90% infill.

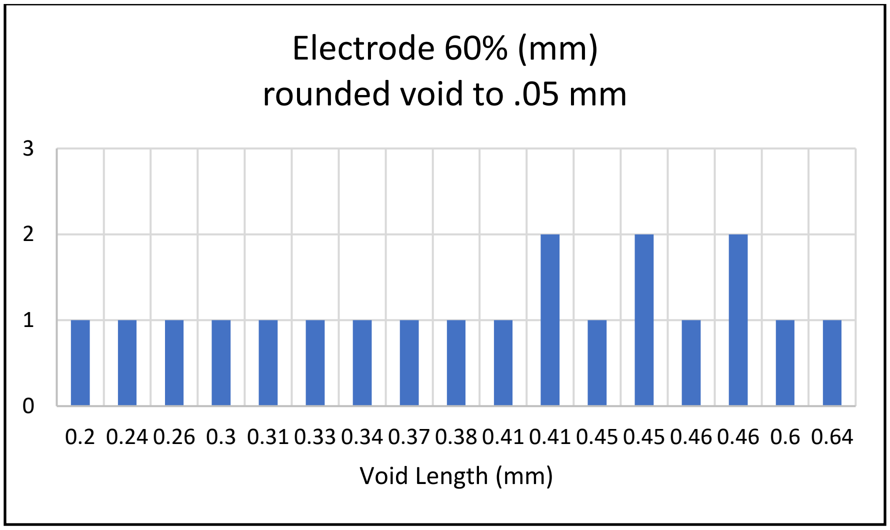

Figure 2.14. Void length analysis of sintered copper electrode with 60% infill.

Section 2.4.4. Scanning Electron Microscope

The SEM analysis was performed to evaluate the surface morphology of the sintered parts. Figure 2.15. displays cross-sectional images of metal fused filament fabricated prints for multiple infill densities. The metal FFF printed parts were studied by increasing the infill density and observing the effects the printing parameter had on its microstructure. In Figure 2.15., the different printed shapes indicate a different infill percentage, where the hexagon indicates a 30% infill density, the circle indicates a 40% infill density, and the square and octagon represent a 60% and 90% infill density, respectively. The increase of gyroid infill percentages resulted in the increase of microstructure density, as anticipated. The micrographs revealed that the sintered parts had a semi-dense microstructure with a lot of pores which provides great potential for electrochemical CO2 reduction activity [56]. In literature, it has been reported that the pores seen in microstructures can enable electron transfer and diffusion needed for electrochemical reactions [57]. The sintered parts also showed fair interparticle bonding [58], indicating that the sintering process was successful. Interparticle bonding was characterized as the necking of two spherical particles that are fused together through heat treatment [59].

The importance of achieving good interparticle bonding is due to the influence the microstructure integrity has on the specimen’s mechanical performance. Poor interparticle bonding can lead to defects in the print, as well as poor mechanical features such as tensile or compressive strength. Tosto et al studied the mechanical properties of FFF printed polymer/metal hybrid prints and analyzed the green and sintered parts using SEM [60]. The micrographs of the hybrid prints showed that the green parts displayed voids and poor interparticle bonding that can result in mechanical failure. Atatreh et al. also investigated the integrity of metal FFF produced parts by analyzing their tensile properties based on infill design [61]. The SEM images showed that the failure modes observed on the tensile tests were contributed to porosity from using the triangle infill patterns versus a solid-filled part. In the case of the micrographs shown in Figure 2.15., the 90% infill density metal parts are anticipated to outperform the other specimens in terms of mechanical properties. Although the 90% infill percentage may exhibit better mechanical performance, this is not necessarily the case for electrochemical activity, where the 60% infill percentage may be more favorable due to its higher exposed surface area which increases the number of active sites available while also facilitating mass transport of reactants, leading to increased reaction rates and efficiencies [52]. However, the nature of the relationship between surface area and reaction rate depends on the specific electrochemical system that is being examined under specific operating conditions.

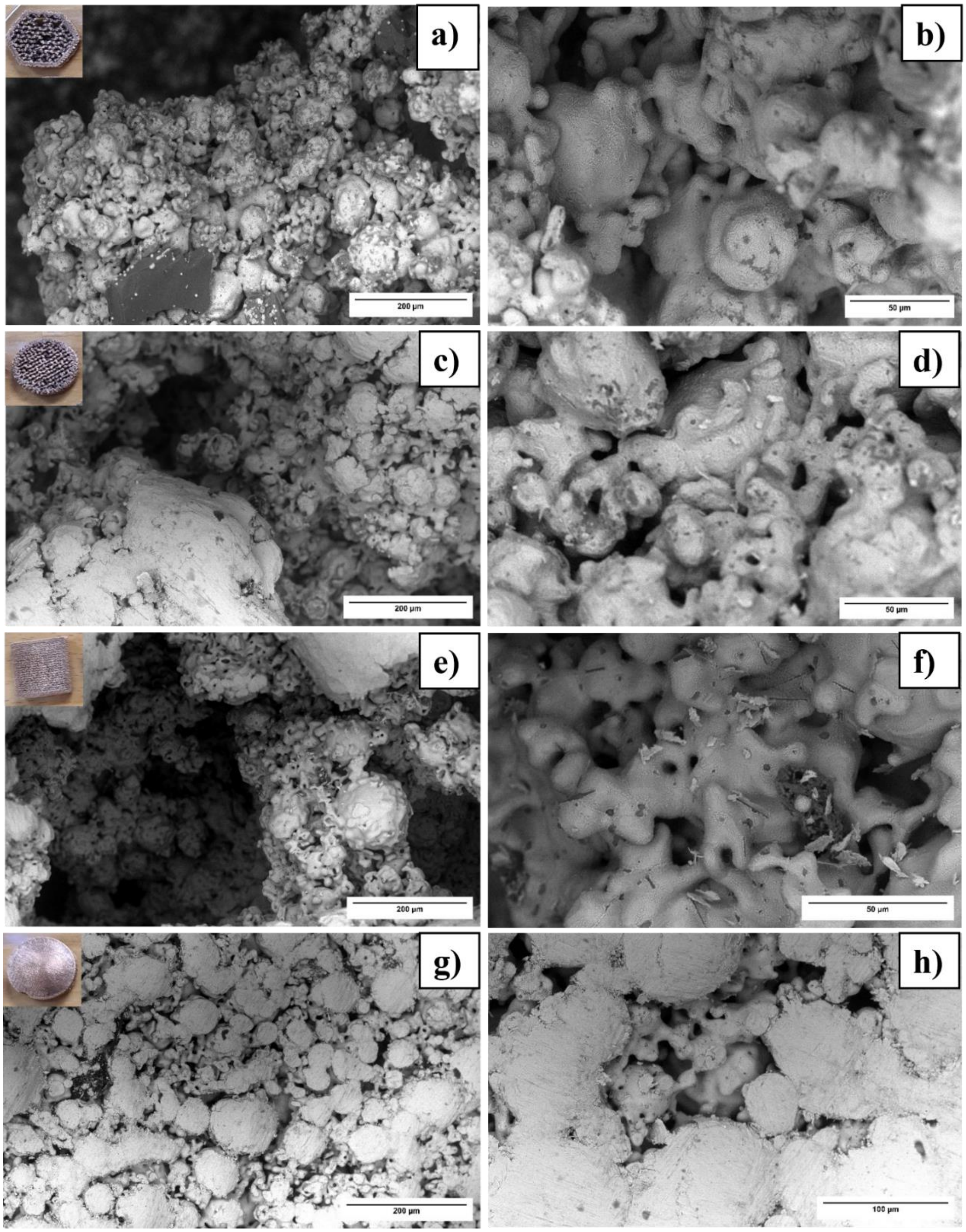

Figure 2.15. SEM micrographs of sintered structures with different gyroid infill percentages. 30 % - 200 um (a), 50 um (b), 40% - 200 um (c), 50 um (d), 60% - 200 um (e), 50 um (f), 90% - 200 um (g), 100 um (h).

Section 2.4.5. Electrochemical reduction of CO_2 - CO and NO_3 - NH_3

The electrochemical reduction of CO_2 to CO and NO_3 to NH_3 is a complex process which has 2 major challenges. A variety of intermediate products are expected in the desired potential range, which can compromise selectivity towards the target product, and high overpotentials favor competing hydrogen evolution reactions at the available active sites [62]. When analyzing the cyclic voltammetry data presented in Figure 2.16., it is apparent that the reduction and oxidation reactions show selectivity at a potential of -0.9 V vs RHE [63] [64]. These results are evaluated in conjunction with other reduction reactions, such as the hydrogen evolution reaction (HER) and nitrate reduction, to assess the selectivity of the copper electrode. In Figure 2.17., the HER reaction exhibits a lower selectivity compared to the CO_2 reduction results, indicating that while these reactions are competitive, the CO_2 reduction shows higher selectivity than HER. On the other hand, Figure 2.18. shows that nitrate reduction exhibits a higher affinity and increased reduction and oxidation, indicating higher selectivity over CO_2 reduction and HER. Nitrate reduction is promising to produce ammonia. Ammonia is a versatile molecule with numerous applications in the energy industry [65]. It can be used as a fuel for power generation in combustion engines, resulting in the production of environmentally friendly byproducts such as nitrogen and water [66]. Additionally, ammonia contains 17.6wt% of hydrogen, making it an ideal medium for hydrogen storage and transportation [67]. Other applications of ammonia include its use in the production of fertilizers, plastics, and as a means of carbon capture and storage [68] [69]. Thus, possessing a higher affinity for ammonia remains advantageous in this context.

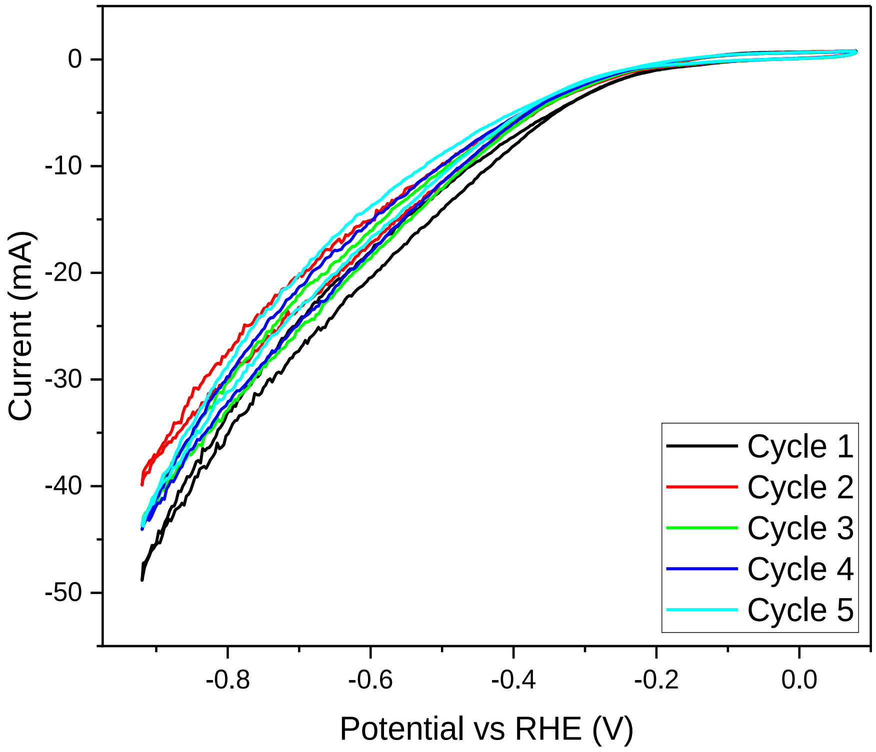

Figure 2.16. Voltammogram of the reversible CO2 reduction of a 0.5M KHCO3 using MF3 sintered copper catalyst, at a scan rate of 10mV/s; Linear Sweep Voltammetry: 2mV/s. CO2 gas purged for 30 minutes. [LA-UR-23-23587] [70]

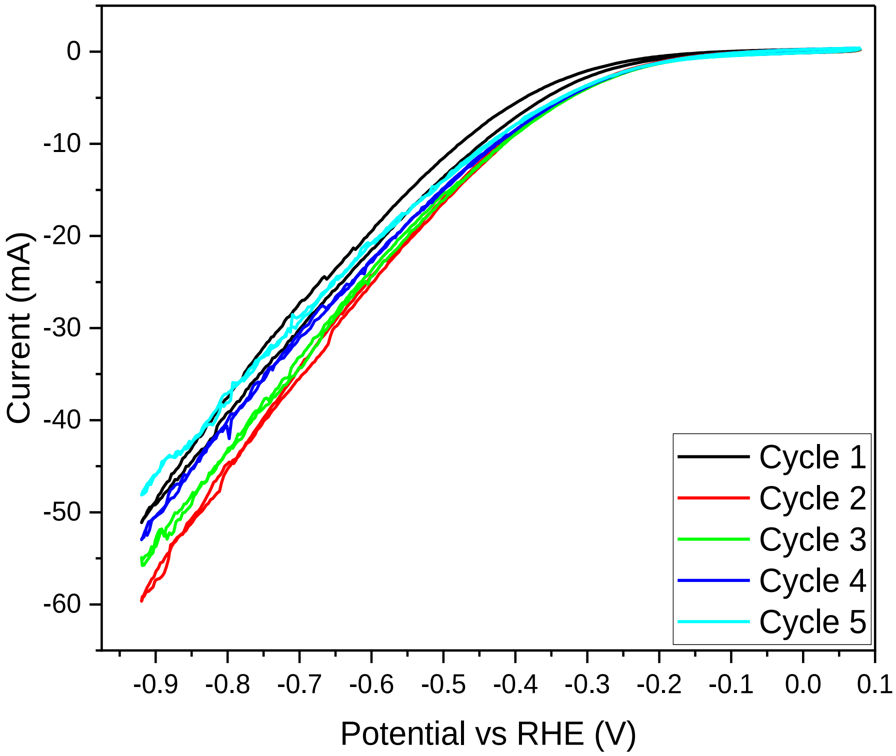

Figure 2.17. Voltammogram of HER of a 0.5M KHCO3 using MF3 sintered copper catalyst, at a scan rate of 10mV/s; Linear Sweep Voltammetry: 2mV/s. N2 gas purged for 30 minutes. [LA-UR-23-23587] [70]

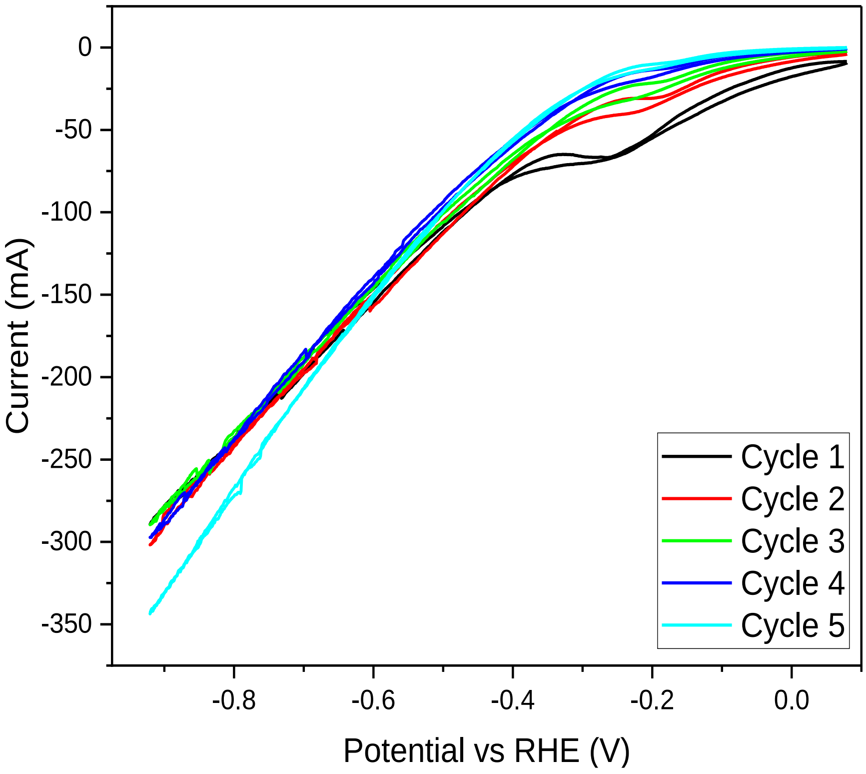

Figure 2.18. Voltammogram of the reversible nitrate reduction of 1M NaOH + 0.1 M NaNO3 using MF3 sintered copper catalyst, at a scan rate of 10mV/s; Linear Sweep Voltammetry: 2mV/s. N2 gas purged for 30 minutes. [LA-UR-23-23587] [70]

Section 2.4.6. nTopology

The study analyzed the dimensional differences between the implicit model, green body, and sintered body. Figure 2.19.b shows the printing orientation. The implicit body measured 32 mm, 32 mm, and 32.25 mm in the print-bed, print-head, and build orientation, respectively. The green body measured 32.18 mm in the print-bed, 31.78 mm in the print-head, and 32.22 mm in the build orientation. The sintered model measured 31.08 mm in the print-bed, 30.96 mm in the print-head, and 28.68 mm in the build orientation. The deviation from the shrinkage was calculated by comparing the measurements of the digital vs green and digital vs sintered. The deviation between the green part and the original part was -0.09% in the build direction, 0.56% in the print-bed, and 2.44% in the print-head. The deviation between the sintered part and the original part was -11.07% in the build direction, -2.88% in the print-bed, and -3.25% in the print-head.

The shrinkage in all directions from the implicit body to the green body may be explained through the resolution of the printer being limited to 0.6 mm due to the nozzle diameter. The high shrinkage experienced on the sintered part on the build direction is due to defects and interlaying gaps caused by the layer-by-layer deposition nature discussed in the density analysis. Nevertheless, nTopology greatly reduces the time required to design complex structures such as TPMS. This significantly materializes the ability to utilize design for additive manufacturing (DfAM) principles, specifically through lattice optimization. This has been shown to enhance mechanical and thermal properties [5]. Employing nTopology can streamline the DfAM pipeline, as it offers simple yet diverse lattice options as well as a suite of simulation software. DfAM, nTopology, and MF3 were combined to fabricate a structure that would be impossible to design conventionally, exploiting the microporosity for electrochemical reduction. Finally, the lattice structure was able to maintain its structure without any major warping or deformation. This enables complex structures to be fabricated with very specific surface area.

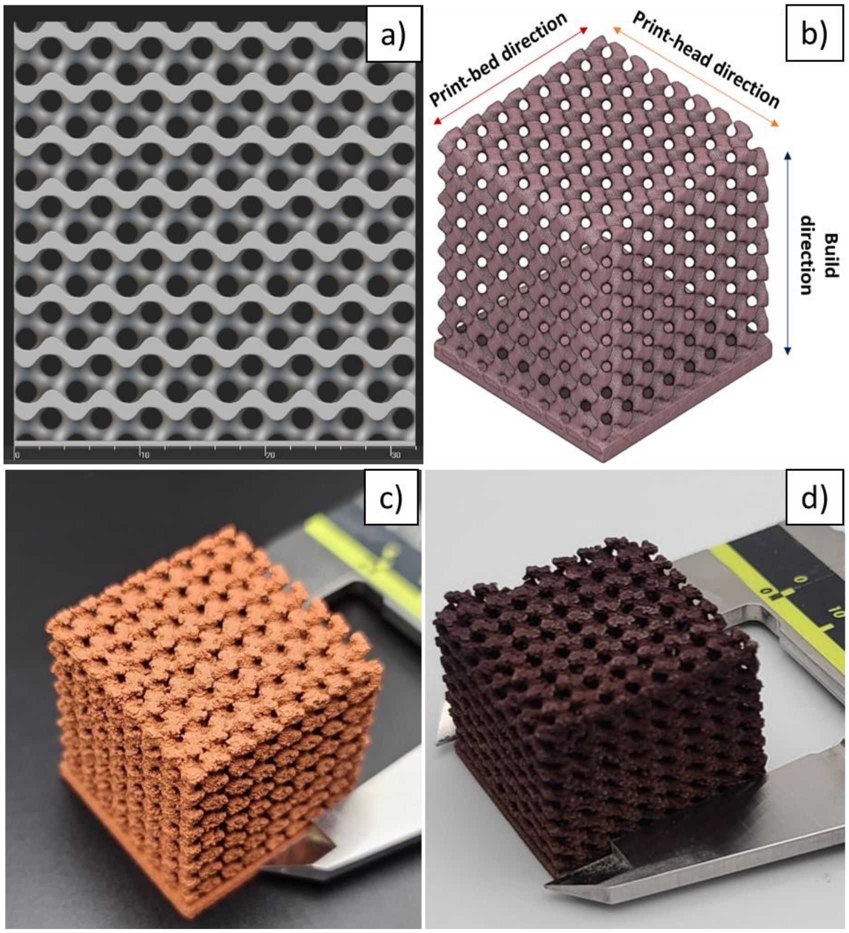

Figure 2.19. nTopology TPMS gyroid lattice structure meshed in nTopology (a), printing orientations (b), Green 3D printed part (b), and sintered part (c)

Section 2.5. Conclusion

This study presents several conclusions that can be drawn based on the experimental and statistical results:

- Overall, the sintered parts achieved densities ranging from 5.12 to 7.72 g/cm3, which is a good indicator for higher active surface area while retaining part integrity.
- The XRD results show crystallinity peaks of Cu in 2θ 43, 50, and 74° which represent (111), (200), and (220) for crystalline orientations respectively and are standard for Cu results that are sintered.
- The pore size diameter recorded ranged from 7 to 22.5 um with an average pore size diameter of 12.5 um.
- Fair interparticle bonding which indicates that the sintering process was successful.
- The total average grain size obtained was 50.76 µm.
- The electrochemical reduction of CO2 using MF3 copper electrodes demonstrated promising results, with comparable performance to what has been reported in the literature.
- The MF3 copper electrodes exhibited a higher affinity for nitrate reduction, which is promising for ammonia production.

Our findings show that MF3 is suitable to manufacture copper components that have a complex porous microstructure that are suitable for CO2 and Nitrate reduction.

References

[1] M. A. Gibson *et al.*, “3D printing metals like thermoplastics: Fused filament fabrication of metallic glasses,” *Materials Today*, vol. 21, no. 7, pp. 697–702, Sep. 2018, doi: 10.1016/j.mattod.2018.07.001.

[2] M. Sadaf, M. Bragaglia, and F. Nanni, “A simple route for additive manufacturing of 316L stainless steel via Fused Filament Fabrication,” *Journal of Manufacturing Processes*, vol. 67, pp. 141–150, Jul. 2021, doi: 10.1016/j.jmapro.2021.04.055.

[3] S. Cano *et al.*, “Additive manufacturing of zirconia parts by fused filament fabrication and solvent debinding: Selection of binder formulation,” *Additive Manufacturing*, vol. 26, pp. 117–128, Mar. 2019, doi: 10.1016/j.addma.2019.01.001.

[4] A. Dey, I. N. Roan Eagle, and N. Yodo, “A Review on Filament Materials for Fused Filament Fabrication,” *Journal of Manufacturing and Materials Processing*, vol. 5, no. 3, Art. no. 3, Sep. 2021, doi: 10.3390/jmmp5030069.

[5] N. Dehdari Ebrahimi and Y. S. Ju, “Thermal conductivity of sintered copper samples prepared using 3D printing-compatible polymer composite filaments,” *Additive Manufacturing*, vol. 24, pp. 479–485, Dec. 2018, doi: 10.1016/j.addma.2018.10.025.

[6] A. Pellegrini, M. E. Palmieri, and M. G. Guerra, “Evaluation of anisotropic mechanical behaviour of 316L parts realized by metal fused filament fabrication using digital image correlation,” *Int J Adv Manuf Technol*, vol. 120, no. 11, pp. 7951–7965, Jun. 2022, doi: 10.1007/s00170-022-09303-z.

[7] C. H. Ji, N. H. Loh, K. A. Khor, and S. B. Tor, “Sintering study of 316L stainless steel metal injection molding parts using Taguchi method: final density,” *Materials Science and Engineering: A*, vol. 311, no. 1, pp. 74–82, Jul. 2001, doi: 10.1016/S0921-5093(01)00942-X.

[8] C. Bellehumeur, L. Li, Q. Sun, and P. Gu, “Modeling of Bond Formation Between Polymer Filaments in the Fused Deposition Modeling Process,” *Journal of Manufacturing Processes*, vol. 6, no. 2, pp. 170–178, Jan. 2004, doi: 10.1016/S1526-6125(04)70071-7.

[9] P. Suri, R. P. Koseski, and R. M. German, “Microstructural evolution of injection molded gas- and water-atomized 316L stainless steel powder during sintering,” *Materials Science and Engineering: A*, vol. 402, no. 1, pp. 341–348, Aug. 2005, doi: 10.1016/j.msea.2005.01.004.

[10] G. Tedla, A. M. Jarabek, P. Byrley, W. Boyes, and K. Rogers, “Human exposure to metals in consumer-focused fused filament fabrication (FFF)/ 3D printing processes,” *Science of The Total Environment*, vol. 814, p. 152622, Mar. 2022, doi: 10.1016/j.scitotenv.2021.152622.

[11] C. Wang, S. Li, D. Zeng, and X. Zhu, “Quantification and compensation of thermal distortion in additive manufacturing: A computational statistics approach,” *Computer Methods in Applied Mechanics and Engineering*, vol. 375, p. 113611, Mar. 2021, doi: 10.1016/j.cma.2020.113611.

[12] S. Afazov, W. A. D. Denmark, B. Lazaro Toralles, A. Holloway, and A. Yaghi, “Distortion prediction and compensation in selective laser melting,” *Additive Manufacturing*, vol. 17, pp. 15–22, Oct. 2017, doi: 10.1016/j.addma.2017.07.005.

[13] S. Sadeghi Borujeni, G. S. Saluja, and V. Ploshikhin, “Compensation of sintering deformation for components manufactured by metal binder jetting using numerical

simulations," *Rapid Prototyping Journal*, vol. 29, no. 3, pp. 612–625, Jan. 2022, doi: 10.1108/RPJ-06-2022-0181.

[14] I. Buj-Corral, A. Bagheri, and M. Sivatte-Adroer, "Effect of Printing Parameters on Dimensional Error, Surface Roughness and Porosity of FFF Printed Parts with Grid Structure," *Polymers*, vol. 13, no. 8, Art. no. 8, Jan. 2021, doi: 10.3390/polym13081213.

[15] S. Afazov, E. Semerdzhieva, D. Scrimieri, A. Serjouei, B. Kairoshev, and F. Derguti, "An improved distortion compensation approach for additive manufacturing using optically scanned data," *Virtual and Physical Prototyping*, vol. 16, no. 1, pp. 1–13, Jan. 2021, doi: 10.1080/17452759.2021.1881702.

[16] M. Li, W. Du, A. Elwany, Z. Pei, and C. Ma, "Metal Binder Jetting Additive Manufacturing: A Literature Review," *Journal of Manufacturing Science and Engineering*, vol. 142, no. 9, Jun. 2020, doi: 10.1115/1.4047430.

[17] S. Banerjee and C. J. Joens, "7 - Debinding and sintering of metal injection molding (MIM) components," in *Handbook of Metal Injection Molding (Second Edition)*, D. F. Heaney, Ed., in Woodhead Publishing Series in Metals and Surface Engineering. Woodhead Publishing, 2019, pp. 129–171. doi: 10.1016/B978-0-08-102152-1.00009-X.

[18] B. Verlee, T. Dormal, and J. Lecomte-Beckers, "Density and porosity control of sintered 316L stainless steel parts produced by additive manufacturing," *Powder Metallurgy*, vol. 55, no. 4, pp. 260–267, Sep. 2012, doi: 10.1179/0032589912Z.00000000082.

[19] R. Yavari, H. Khorsand, and M. Sardarian, "Simulation and modeling of macro and micro components produced by powder injection molding: A review," *Polyolefins Journal*, vol. 7, no. 1, pp. 45–60, Dec. 2019, doi: 10.22063/poj.2019.2568.1141.

[20] S. Sadeghi Borujeni, G. S. Saluja, and V. Ploshikhin, "Compensation of sintering deformation for components manufactured by metal binder jetting using numerical simulations," *Rapid Prototyping Journal*, vol. 29, no. 3, pp. 612–625, Jan. 2022, doi: 10.1108/RPJ-06-2022-0181.

[21] "Standard Test Methods for Density of Compacted or Sintered Powder Metallurgy (PM) Products Using Archimedes' Principle." https://www.astm.org/b0962-17.html (accessed Apr. 15, 2023).

[22] D. A. Ramirez *et al.*, "Open-cellular copper structures fabricated by additive manufacturing using electron beam melting," *Materials Science and Engineering: A*, vol. 528, no. 16, pp. 5379–5386, Jun. 2011, doi: 10.1016/j.msea.2011.03.053.

[23] Y. Thompson, J. Gonzalez-Gutierrez, C. Kukla, and P. Felfer, "Fused filament fabrication, debinding and sintering as a low cost additive manufacturing method of 316L stainless steel," *Additive Manufacturing*, vol. 30, p. 100861, Dec. 2019, doi: 10.1016/j.addma.2019.100861.

[24] T. Q. Tran *et al.*, "3D Printing of Highly Pure Copper," *Metals*, vol. 9, no. 7, Art. no. 7, Jul. 2019, doi: 10.3390/met9070756.

[25] A. Y. Al-Maharma, S. P. Patil, and B. Markert, "Effects of porosity on the mechanical properties of additively manufactured components: a critical review," *Mater. Res. Express*, vol. 7, no. 12, p. 122001, Dec. 2020, doi: 10.1088/2053-1591/abcc5d.

[26] I. Ait-Mansour, N. Kretzschmar, S. Chekurov, M. Salmi, and J. Rech, "Design-dependent shrinkage compensation modeling and mechanical property targeting of metal FFF," *Prog Addit Manuf*, vol. 5, no. 1, pp. 51–57, Mar. 2020, doi: 10.1007/s40964-020-00124-8.

[27] G. R. M, "Theory of thermal debinding," *Int. J. Powder Metall.*, vol. 23, pp. 237–245, 1987.

[28] Y. Shengjie, Y. C. Lam, S. C. M. Yu, and K. C. Tam, “Thermal debinding modeling of mass transport and deformation in powder-injection molding compact,” *Metall Mater Trans B*, vol. 33, no. 3, pp. 477–488, Jun. 2002, doi: 10.1007/s11663-002-0058-6.

[29] M. Afifeh, S. J. Hosseinipour, and R. Jamaati, “Manufacturing of pure copper with extraordinary strength-ductility-conductivity balance by cryorolling and annealing,” *CIRP Journal of Manufacturing Science and Technology*, vol. 37, pp. 623–632, May 2022, doi: 10.1016/j.cirpj.2022.03.010.

[30] B. Rath, M. Imam, and C. Pande, “Nucleation and growth of twin interfaces in fcc metals and alloys.,” *Mater. Phys. Mech*, pp. 61–66, 2000.

[31] R. Bidulský, J. Bidulská, and M. Actis Grande, “Analysis of Densification Process and Structure of PM Al-Mg-Si-Cu-Fe and Al-Zn-Mg-Cu-Sn Alloys,” *Archives of Metallurgy and Materials*, vol. Vol. 59, iss. 1, 2014, doi: 10.2478/amm-2014-0003.

[32] S. Chintada, S. P. Dora, and D. Kare, “Mechanical Behavior and Metallographic Characterization of Microwave Sintered Al/SiC Composite Materials – an Experimental Approach,” *Silicon*, vol. 14, no. 12, pp. 7341–7352, Aug. 2022, doi: 10.1007/s12633-021-01409-5.

[33] Q. Li *et al.*, “Balancing flexural strength and porosity in DLP-3D printing Al2O3 cores for hollow turbine blades,” *Journal of Materials Science & Technology*, vol. 104, pp. 19–32, Mar. 2022, doi: 10.1016/j.jmst.2021.05.077.

[34] “Effects of porosity on the mechanical properties of additively manufactured components: a critical review - IOPscience.” https://iopscience.iop.org/article/10.1088/2053-1591/abcc5d/meta (accessed Apr. 14, 2023).

[35] J. Duan *et al.*, “Controlled crystallinity and crystallographic orientation of Cu nanowires fabricated in ion-track templates,” *Nanotechnology*, vol. 21, no. 36, p. 365605, Aug. 2010, doi: 10.1088/0957-4484/21/36/365605.

[36] C.-H. Ryu, S.-J. Joo, and H.-S. Kim, “Two-step flash light sintering of copper nanoparticle ink to remove substrate warping,” *Applied Surface Science*, vol. 384, pp. 182–191, Oct. 2016, doi: 10.1016/j.apsusc.2016.05.025.

[37] N. A. M. Shanid and M. A. Khadar, “Evolution of nanostructure, phase transition and band gap tailoring in oxidized Cu thin films,” *Thin Solid Films*, vol. 516, no. 18, pp. 6245–6252, Jul. 2008, doi: 10.1016/j.tsf.2007.11.119.

[38] “Oxidation mechanism of thin Cu films: A gateway towards the formation of single oxide phase: AIP Advances: Vol 8, No 5.” https://aip.scitation.org/doi/full/10.1063/1.5028407 (accessed Apr. 14, 2023).

[39] A. Cattenone, S. Morganti, G. Alaimo, and F. Auricchio, “Finite Element Analysis of Additive Manufacturing Based on Fused Deposition Modeling: Distortions Prediction and Comparison With Experimental Data,” *Journal of Manufacturing Science and Engineering*, vol. 141, no. 1, Nov. 2018, doi: 10.1115/1.4041626.

[40] S. Sadeghi Borujeni, G. S. Saluja, and V. Ploshikhin, “Compensation of sintering deformation for components manufactured by metal binder jetting using numerical simulations,” *Rapid Prototyping Journal*, vol. 29, no. 3, pp. 612–625, Jan. 2022, doi: 10.1108/RPJ-06-2022-0181.

[41] E. Vaněčková *et al.*, “Electrochemical Reduction of Carbon Dioxide on 3D Printed Electrodes,” *ChemElectroChem*, vol. 8, no. 11, pp. 2137–2149, 2021, doi: 10.1002/celc.202100261.

[42] D. M. Wirth *et al.*, "Electrolysis Activation of Fused-Filament-Fabrication 3D-Printed Electrodes for Electrochemical and Spectroelectrochemical Analysis," *Anal. Chem.*, vol. 91, no. 9, pp. 5553–5557, May 2019, doi: 10.1021/acs.analchem.9b01331.

[43] "CO2 Emissions in 2022 – Analysis," *IEA*. https://www.iea.org/reports/co2-emissions-in-2022 (accessed Apr. 30, 2023).

[44] L. Jeffry, M. Y. Ong, S. Nomanbhay, M. Mofijur, M. Mubashir, and P. L. Show, "Greenhouse gases utilization: A review," *Fuel*, vol. 301, p. 121017, Oct. 2021, doi: 10.1016/j.fuel.2021.121017.

[45] K. Kaygusuz, "Energy for Sustainable Development: Key Issues and Challenges," *Energy Sources, Part B: Economics, Planning, and Policy*, vol. 2, no. 1, pp. 73–83, Apr. 2007, doi: 10.1080/15567240500402560.

[46] J. Lim, C. A. Fernández, S. W. Lee, and M. C. Hatzell, "Ammonia and Nitric Acid Demands for Fertilizer Use in 2050," *ACS Energy Lett.*, vol. 6, no. 10, pp. 3676–3685, Oct. 2021, doi: 10.1021/acsenergylett.1c01614.

[47] H. Karcher, K. Polthier, J. Klinowski, and A. L. Mackay, "Construction of triply periodic minimal surfaces," *Philosophical Transactions of the Royal Society of London. Series A: Mathematical, Physical and Engineering Sciences*, vol. 354, no. 1715, pp. 2077–2104, Jan. 1997, doi: 10.1098/rsta.1996.0093.

[48] H. Xu, Y. M. Xie, R. Chan, and S. Zhou, "Piezoelectric properties of triply periodic minimum surface structures," *Composites Science and Technology*, vol. 200, p. 108417, Nov. 2020, doi: 10.1016/j.compscitech.2020.108417.

[49] P. Tran and P. Chenxi, "Triply periodic minimal surfaces sandwich structures subjected to shock impact - Phuong Tran, Chenxi Peng, 2021." https://journals.sagepub.com/doi/full/10.1177/1099636220905551 (accessed Apr. 30, 2023).

[50] S. Catchpole-Smith, R. R. J. Sélo, A. W. Davis, I. A. Ashcroft, C. J. Tuck, and A. Clare, "Thermal conductivity of TPMS lattice structures manufactured via laser powder bed fusion," *Additive Manufacturing*, vol. 30, p. 100846, Dec. 2019, doi: 10.1016/j.addma.2019.100846.

[51] R. Daiyan, W. H. Saputera, H. Masood, J. Leverett, X. Lu, and R. Amal, "A Disquisition on the Active Sites of Heterogeneous Catalysts for Electrochemical Reduction of CO2 to Value-Added Chemicals and Fuel," *Advanced Energy Materials*, vol. 10, no. 11, p. 1902106, 2020, doi: 10.1002/aenm.201902106.

[52] S. Jin, Z. Hao, K. Zhang, Z. Yan, and J. Chen, "Advances and Challenges for the Electrochemical Reduction of CO2 to CO: From Fundamentals to Industrialization," *Angewandte Chemie*, vol. 133, no. 38, pp. 20795–20816, 2021, doi: 10.1002/ange.202101818.

[53] K. Dash, B. C. Ray, and D. Chaira, "Synthesis and characterization of copper–alumina metal matrix composite by conventional and spark plasma sintering," *Journal of Alloys and Compounds*, vol. 516, pp. 78–84, Mar. 2012, doi: 10.1016/j.jallcom.2011.11.136.

[54] H.-S. Kim, S. R. Dhage, D.-E. Shim, and H. T. Hahn, "Intense pulsed light sintering of copper nanoink for printed electronics," *Appl. Phys. A*, vol. 97, no. 4, pp. 791–798, Dec. 2009, doi: 10.1007/s00339-009-5360-6.

[55] M. Q. Shaikh *et al.*, "Investigation of Patient-Specific Maxillofacial Implant Prototype Development by Metal Fused Filament Fabrication (MF3) of Ti-6Al-4V," *Dentistry Journal*, vol. 9, no. 10, Art. no. 10, Oct. 2021, doi: 10.3390/dj9100109.

[56] W. Guo, K. Shim, F. O. Odongo Ngome, Y. H. Moon, S.-Y. Choi, and Y.-T. Kim, “Highly active coral-like porous silver for electrochemical reduction of CO2 to CO,” *Journal of CO2 Utilization*, vol. 41, p. 101242, Oct. 2020, doi: 10.1016/j.jcou.2020.101242.

[57] H. Ma, Y. Chen, X. Li, and B. Li, “Advanced Applications and Challenges of Electropolymerized Conjugated Microporous Polymer Films,” *Advanced Functional Materials*, vol. 31, no. 33, p. 2101861, 2021, doi: 10.1002/adfm.202101861.

[58] Y. Bai and C. B. Williams, “An exploration of binder jetting of copper,” *Rapid Prototyping Journal*, vol. 21, no. 2, pp. 177–185, Jan. 2015, doi: 10.1108/RPJ-12-2014-0180.

[59] J. Yao, H. Dong, Y. Li, and X. Li, “Influence of Inter-Particle Bonding on Compression Performance of Porous Mo Deposited by Flame Spraying of Semi-Molten Particles,” *Coatings*, vol. 9, no. 3, Art. no. 3, Mar. 2019, doi: 10.3390/coatings9030158.

[60] C. Tosto, J. Tirillò, F. Sarasini, and G. Cicala, “Hybrid Metal/Polymer Filaments for Fused Filament Fabrication (FFF) to Print Metal Parts,” *Applied Sciences*, vol. 11, no. 4, Art. no. 4, Jan. 2021, doi: 10.3390/app11041444.

[61] S. Atatreh, M. S. Alyammahi, H. Vasilyan, T. Alkindi, and R. A. Susantyoko, “Evaluation of the infill design on the tensile properties of metal parts produced by fused filament fabrication,” *Results in Engineering*, vol. 17, p. 100954, Mar. 2023, doi: 10.1016/j.rineng.2023.100954.

[62] J. S. Yoo, R. Christensen, T. Vegge, J. K. Nørskov, and F. Studt, “Theoretical Insight into the Trends that Guide the Electrochemical Reduction of Carbon Dioxide to Formic Acid,” *ChemSusChem*, vol. 9, no. 4, pp. 358–363, 2016, doi: 10.1002/cssc.201501197.

[63] S. Nitopi *et al.*, “Progress and Perspectives of Electrochemical CO2 Reduction on Copper in Aqueous Electrolyte,” *Chem. Rev.*, vol. 119, no. 12, pp. 7610–7672, Jun. 2019, doi: 10.1021/acs.chemrev.8b00705.

[64] C. S. Le Duff, M. J. Lawrence, and P. Rodriguez, “Role of the Adsorbed Oxygen Species in the Selective Electrochemical Reduction of CO2 to Alcohols and Carbonyls on Copper Electrodes,” *Angewandte Chemie*, vol. 129, no. 42, pp. 13099–13104, 2017, doi: 10.1002/ange.201706463.

[65] P. H. van Langevelde, I. Katsounaros, and M. T. M. Koper, “Electrocatalytic Nitrate Reduction for Sustainable Ammonia Production,” *Joule*, vol. 5, no. 2, pp. 290–294, Feb. 2021, doi: 10.1016/j.joule.2020.12.025.

[66] A. Sánchez, E. Castellano, M. Martín, and P. Vega, “Evaluating ammonia as green fuel for power generation: A thermo-chemical perspective,” *Applied Energy*, vol. 293, p. 116956, Jul. 2021, doi: 10.1016/j.apenergy.2021.116956.

[67] A. Klerke, C. Hviid Christensen, J. K. Nørskov, and T. Vegge, “Ammonia for hydrogen storage: challenges and opportunities,” *Journal of Materials Chemistry*, vol. 18, no. 20, pp. 2304–2310, 2008, doi: 10.1039/B720020J.

[68] “Ammonia in agriculture: The engine of plant growth,” *thyssenkrupp*. https://www.thyssenkrupp.com/en/stories/sustainability-and-climate-protection/ammonia-in-agriculture:-the-engine-of-plant-growth (accessed May 01, 2023).

[69] K. H. M. Al-Hamed and I. Dincer, “A comparative review of potential ammonia-based carbon capture systems,” *Journal of Environmental Management*, vol. 287, p. 112357, Jun. 2021, doi: 10.1016/j.jenvman.2021.112357.

[70] “2023, Los Alamos National Laboratory, NM, LA-UR-23-23587.”

Vita

Mr. Montes began his college education at The University of Texas at El Paso (UTEP) where he obtained a Bachelor's degree in Mechanical Engineering in the Fall of 2017. In the Spring of 2018, he was admitted to the Biomedical Engineering Master's program at UTEP and joined Dr. Fatima Alshbool's laboratory in the Department of Pharmaceutical Sciences, School of Pharmacy. During his master's degree, Jean studied cardiovascular disease, specifically thrombosis-based diseases, and focused on modulating platelet function.

During his master's degree, Mr. Montes researched the health safety profile of JUUL, a popular electronic cigarette (e-cigarettes) in the U.S. Additionally, Mr. Montes also worked with a novel antibody targeting the serotonin-receptor 5HT2AR ligand binding domain to confirm its potential use as an antithrombotic agent.

Since then, Mr. Montes was admitted into the Mechanical Engineering Doctorate program where he joined Dr. Yirong Lin with the department of Mechanical Engineering at UTEP. During his doctorate degree, he obtained a Master's degree in Mechanical Engineering and an Additive Manufacturing Certificate. His doctorate research mainly focused on Metal Fused Filament Fabrication, embedded sensing, non-destructive testing, and metal additive manufacturing.

Mr. Montes is a skilled researcher with expertise in cardiovascular disease, metal additive manufacturing, embedded sensing, and non-destructive testing. With a strong work ethic and a passion for innovation, his diverse curriculum makes him well-equipped to excel in industry and make significant contributions to his field.

Contact Information: jemontesramirez@gmail.com